LAWRENCE
LIVERMORE
NATIONAL
LABORATORY

UCRL-JRNL-224121

Lightcurves of Type Ia Supernovae from Near the Time of Explosion

A. Garg, C. W. Stubbs, P. Challis, M. Wood-Vasey, S. Blondin, M. E. Huber, K. Cook, S. Nikolaev, A. Rest, R. C. Smith, K. Olsen, N. B. Suntzeff, C. Aguilera, J. L. Prieto, A. Becker, A. Miceli, G. Miknaitis, A. Clocchiatti, D. Minniti, L. Morelli, D. Welch

August 31, 2006

Astronomical Journal

Disclaimer

Lightcurves of Type Ia Supernovae from Near the Time of Explosion

Arti Garg[1]

artigarg@fas.harvard.edu

Christopher W. Stubbs[1], Peter Challis[1], W. Michael Wood-Vasey[1], and Stéphane Blondin[1]

Department of Physics and Harvard-Smithsonian Center for Astrophysics
Harvard University, Cambridge MA USA

Mark E. Huber[1], Kem Cook[1], and Sergei Nikolaev

Lawrence Livermore National Laboratory

Armin Rest[2], R. Chris Smith, Knut Olsen, Nicholas B. Suntzeff, and Claudio Aguilera

Cerro Tololo Inter-American Observatory/NOAO[3]

Jose Luis Prieto[1]

Ohio State University

Andrew Becker[1] and Antonino Miceli

University of Washington

Gajus Miknaitis[1]

Fermi National Accelerator Laboratory

Alejandro Clocchiatti[1], Dante Minniti, and Lorenzo Morelli[1]

P. Universidad Catolica

Douglas L. Welch[1]

McMaster University

---

[1]Visiting Astronomer, Cerro Tololo Inter-American Observatory, National Optical Astronomy Observatory, which is operated by the Association of Universities for Research in Astronomy, Inc. (AURA) under cooperative agreement with the National Science Foundation

[2]Goldberg fellow

[3]Cerro Tololo Inter-American Observatory, National Optical Astronomy Observatory, which is operated by the Association of Universities for Research in Astronomy, Inc. (AURA) under cooperative agreement with the National Science Foundation

ABSTRACT

We present a set of 11 type Ia supernova (SN Ia) lightcurves with dense, pre-maximum sampling. These supernovae (SNe), in galaxies behind the Large Magellanic Cloud (LMC), were discovered by the SuperMACHO survey. The SNe span a redshift range of z = 0.11 – 0.35. Our lightcurves contain some of the earliest pre-maximum observations of SNe Ia to date. We also give a functional model that describes the SN Ia lightcurve shape (in our VR-band). Our function uses the "expanding fireball" model of Goldhaber et al. (1998) to describe the rising lightcurve immediately after explosion but constrains it to smoothly join the remainder of the lightcurve. We fit this model to a composite observed VR-band lightcurve of three SNe between redshifts of 0.135 to 0.165. These SNe have not been K-corrected or adjusted to account for reddening. In this redshift range, the observed VR-band most closely matches the rest frame V-band. Using the best fit to our functional description of the lightcurve, we find the time between explosion and observed VR-band maximum to be $19.2\pm1.3-1.6\pm0.07$*(red.)* rest-frame days for a SN Ia with a VR-band Δm_{-10} of 0.52. For the redshifts sampled, the observed VR-band time-of-maximum brightness should be the same as the rest-frame V-band maximum to within 1.1 rest-frame days.

Subject headings: surveys—supernovae: general—Magellanic Clouds—*Facilities:* Blanco (), Magellan:Baade (), Magellan:Clay ()

1. Introduction

1.1. Rise-time as a tool to discriminate between SN Ia explosion models

The realization that type Ia supernovae (SNe Ia) can be used as standardizable candles (Phillips 1993; Riess et al. 1995, 1996; Hamuy et al. 1996, 1996b) led to an explosion in SN Ia science. Surveys to test the Hubble Expansion Law at larger distances found that rather than exhibiting a constant or decelerating expansion rate, the Universe has an accelerating expansion (Riess et al. 1998, Perlmutter et al. 1999). The consensus explanation for the accelerating expansion is a negative pressure, or dark energy, permeating the Universe. Today many teams are working to use SNe Ia as standard candles to better constrain the properties of dark energy (ESSENCE, Matheson et al. 2005; SCP, Kowalski et al. 2005; SNLS, Astier et al. 2006). While the methods to standardize the SN Ia luminosity vary, the interpretation of all their results rely to varying degrees on the basic assumption that SNe Ia belong to a single-parameter family.

Methods of standardizing SN Ia luminosity distance using the post-maximum lightcurve shape have proven successful when verified against other standard candles such as Cepheids (Suntzeff et al. 1999, Gibson et al. 2000). These results do not necessarily indicate the existence of a single-parameter family of progenitors, only that the behavior of SNe Ia post-maximum is similar. Still, the most widely considered SN Ia progenitors are carbon-oxygen (C-O) white dwarfs in binary systems. Even accepting these systems as the progenitors, questions remain concerning the mechanism and progression of the explosion. Many competing theories (see Hillebrandt & Niemeyer 2000 and references therein) predict roughly the same post-maximum behavior and vary only in the prediction of the pre-maximum, or rising, lightcurves and spectra. Understanding the explosion mechanism may help us better understand how the population of SNe Ia, and their progenitors, evolves over cosmological time. Many explosion models are sensitive to element abundances in the progenitors and also to progenitor environments. Combining existing information about the differences between low- and high-z stellar populations and galaxies with a more accurate model of the SN Ia explosion mechanism will help more tightly constrain the impact of evolution on SN Ia lightcurve shape. Discriminating between competing explosion models, however, requires lightcurve coverage close to the time of explosion which has been scarcely available.

The reasons for the lack of early pre-maximum lightcurve coverage are many-fold. Some SNe Ia searches rely on a search-and-follow method where SNe are discovered and then followed by another, larger telescope. Discovery often occurs near maximum brightness, and dense pre-maximum temporal coverage is not available. Other surveys, similar to SuperMACHO, revisit the same fields every few days, obtaining consistent temporal coverage over the entire lightcurve. These data sets have better pre-maximum coverage but still do not generally provide densely-sampled pre-maximum lightcurves. In order to maximize the number of fields observed, most surveys use a long, multi-day gap between observations which is sufficient to standardize the post-maximum behavior but often misses the earliest portion of the rise. For higher-z SNe where the multi-day gap between observations translates to a shorter gap in the SN's rest-frame, the earliest portion of the rise is often too faint to be observed. As described more completely below, the SuperMACHO data avoid these two pitfalls. This survey provides dense coverage (every other night) and deep imaging with its custom, broadband VR filter.

1.2. SuperMACHO and Supernova detection

The SuperMACHO project is a five-year optical survey of the Large Magellanic Cloud (LMC) aimed at detecting microlensing of LMC stars (Stubbs et al. 2002). The goal of

this survey is to determine the location of the lens population responsible for the excess microlensing rate observed toward the LMC by the MACHO project (see Alcock et al. 2000 and references therein) and, thereby, better constrain the fraction of MAssive Compact Halo Objects (MACHOs) in the Galactic halo. The survey is conducted on the CTIO Blanco 4m telescope using a custom VR broadband filter. SuperMACHO observes 68 LMC fields during dark and gray time in the months of October – December. We completed our fifth season of observations in the second half of 2005. We process our images with a near-real time data reduction pipeline that employs a difference-imaging technique (see Alard & Lupton 1998, Alcock et al. 1999, Alard 2000, and Gössl 2002) which enables us to detect small changes in flux and to produce lightcurves uncontaminated by light from nearby, non-varying sources.

We present here a uniform set of densely sampled pre-maximum SNe Ia lightcurves from the SuperMACHO survey. From these we constrain the minimum time to maximum brightness for SNe Ia. We present data to provide constraints on SN Ia explosion models to aid in discriminating between competing theories. In Section 2 we discuss our observations. In Section 3 we present our data. In Section 4 we use our data to place limits on the time to maximum brightness and present a functional model for the SN Ia lightcurve shape.

2. Observations

2.1. Imaging

The lightcurves of the sources we report were obtained on the CTIO Blanco 4m telescope during the 2004 season of the SuperMACHO survey. The images were taken using the MOSAIC II wide-field CCD camera. With a plate scale of 0.27"/pixel, MOSAIC II's 8 SITe 2Kx4k CCDs cover a 0.32 sq. deg. field. On a given night we image approximately 60 of our 68 fields so that we obtain relatively dense time-coverage of the events we detect. All survey images are taken in a single, custom VR passband (see Figure 1 for transmission curve). This broad filter enables us to detect flux excursions while they are still too faint for many narrower filters to detect at high S/N. We use an Atmospheric Dispersion Corrector (ADC) to suppress the atmospheric dispersion through our broad filter. A detailed description of the data reduction pipeline and event selection criteria will be available in Rest et al. (2007, in preparation) and Garg et al. (2007, in preparation).

The images are processed using a near real-time pipeline. SuperMACHO surveys 50 million sources. The difference-imaging technique we use enables us to limit our attention to a subset of those lightcurves that includes only those that show changes in brightness. We identify candidate events by first choosing, from previous years' data, the highest quality

image for each field to create a set of templates. We then subtract the templates from the co-registered detection images to produce "difference images" showing only sources whose brightness has varied since the template epoch. This difference-imaging technique enables improved sensitivity to faint flux excursions, particularly in crowded fields such as those in the LMC. We consider any difference flux detections coincident within a 1x1 pixel box in all images of a field to be from a single source and so caused by a unique flux excursion event. We obtain a difference lightcurve for each flux excursion event by measuring the difference flux under a point-source function whose center is forced to be at the centroid of all the difference image detections clustered within that box. By performing this "forced difference flux photometry" on all images of an event location, we measure changes in difference flux that are below a triggering threshold of S/N > 5.

Each night's data reveal hundreds of optically varying events. The majority of these are due to intrinsically variable stars, detector artifacts, cosmic rays, and diffraction spikes from nearby bright stars. To limit the set of lightcurves to unique flux excursions (such as microlensing, AGN activity, and supernovae) of real sources, a series of cuts are applied to the lightcurves. These include the significance of the measured difference flux and goodness-of-fit to a flat baseline in years prior to the event. Known variable sources in the MACHO catalog and sources with more than 3 difference detections of S/N > 10 in previous years are removed from the set. Finally, all remaining lightcurves and their associated detection and difference images are inspected by eye to remove spurious detections caused by artifacts. This selection process whittles the set of new candidate transient events discovered each night of the survey to approximately 20. Fits to models of microlensing and SN Ia lightcurves and visual inspection of template and difference images (for the appearance of host galaxies) are used to preliminarily categorize the events as microlensing, supernovae, AGN's, or other optical transients. The events are then placed in a queue for spectroscopic confirmation (see Section 2.2).

The final lightcurves we present in this paper were produced using the N(N-1)/2 method (hereafter "NN2") of Barris et al. (2005). With this method, instead of using a single template, we difference all possible image pairs to produce the final lightcurve whose points are weighted combinations of the difference flux in all subtractions for a given observation. We use NN2 subtractions to provide cleaner difference lightcurves for our SNe which are behind very crowded LMC fields and often close to other variable sources.

2.2. Spectroscopy

Both Magellan telescopes, Clay and Baade, were used to to obtain spectroscopic follow-up of events identified by the CTIO 4m. On the Clay Telescope, the Low Dispersion Survey Spectrograph 2 (LDSS2; Allington-Smith et al., 1994) was used to obtain longslit spectroscopy on our targets. The LDSS2 CCD detector has a resolution of 0.378"/pixel. We used the following configuration for the spectra obtained on this instrument: the medium resolution (300 l/mm) blue grism blazed at 5000Å, a slit of 0.75", and no blocking filter. The spectra have a nominal dispersion of 5.3Å/pix over the useful wavelength range of ∼3800–7500Å. On the Baade Telescope, we used the Inamori-Magellan Areal Camera and Spectrograph (IMACS; Bigelow & Dressler, 2003) in longslit mode with the long camera (f/4 focus) and the medium resolution, 300 l/mm, grating. In this configuration the instrument provides a 0.111"/pix image scale with a nominal dispersion of 0.743Å/pix over a useful wavelength span of 3800–7500Å without order blocking filters. The nights were mostly photometric and the Shack-Hartmann wavefront sensor provided image qualities of ∼0.6"–1.1" FWHM. To minimize slit losses due to atmospheric dispersion, we used a slit aligned to the parallactic angle. Observations typically consisted of multiple integrations on a source. The S/N on each target varied with the integration times, source brightness, transparency, and seeing.

Reduction of the spectra consists of the typical single slit processing using standard IRAF routines for bias subtraction and flat-fielding. Cosmic ray removal is facilitated using the Laplacian Cosmic Ray identification routine of van Dokkum (2001). We co-add the processed 2D images of each target and extract 1D apertures using isolated regions around the target source for the background subtraction. We determine the best 1D extraction by iterating through multiple target and sky regions to ensure proper source and sky isolation within the crowded LMC fields. We find the dispersion solution for each image using He Ne Ar arc lamp observations that show a typical RMS of <0.5Å. We use spectrophotometric standards (Feige 110, Hiltner 600, and LTT3864) observed on the same night as the targets for flux calibratation.

3. Data

3.1. Lightcurves

We present 11 SNe Ia from the 2004 observing season. Table 1 gives their positions and redshifts. Tables 2–12 give the lightcurves for each object. The NN2 difference fluxes in the lightcurves are given normalized to a zero point of 25 (see Rest et al. 2005 for VR-band

standardization procedure). Figures 2–6 show the lightcurves with the time axis transformed to the SN rest-frame and relative to the time of maximum brightness in the observed VR-band, t_{max} (see Section 4.2 for t_{max} determination procedure). We normalize the observed fluxes to the flux at maximum, VR_{max} to obtain the $\frac{f_{VR}}{VR_{max}}$ lightcurves shown. The SNe are grouped by redshift, and each figure shows all SNe with similar redshifts (see Section 3.2 for redshift determination procedure). We group the SNe Ia by redshift to limit the impact of K-corrections (Hamuy et al. 1993, Kim et al. 1996, Schmidt et al. 1998, and Nugent et al. 2002) on our findings (see 4.3.1 for further discussion of K-corrections).

3.2. Spectra

Table 13 lists the telescope, instrument, observation date, and total integration time for each spectrum presented. We determine the SN type and redshift by comparing the spectrum to a library of nearby SN spectra (Matheson et al. 2006, in preparation). Following the method of Matheson et al. (2005) we classify an event as a SN Ia if it shows the characteristic CaII H&K, SiII, FeII, and SII features (Filippenko 1997). We choose a comparison spectrum from the nearby library that was obtained at approximately the same SN phase as our spectrum. We determine the object's redshift by redshifting the nearby spectrum until the peaks and valleys match. This gives z to an accuracy of $\sim$0.01. Because we do not apply Galactic, LMC, or host galaxy reddening corrections, the continuum shapes of our spectra sometimes appear flatter and redder than that of the nearby, reddening-corrected spectrum. Figures 7–17 show the spectrum of each SN with the redshifted nearby comparison spectrum above. The SN's redshift determined by this method is given in Table 1.

Three of the spectra also exhibit strong host galaxy emission and absorption features. We use these features to obtain more accurate redshifts for these sources and to verify the nearby SN comparison method of redshift determination used for the remaining SNe. To determine the galactic redshifts we first find the line centers of the emission and absorption features by fitting a Gaussian profile to each. We then calculate the galaxy's redshift by averaging the redshifts of the identified lines. Table 14 lists the SNe whose spectra exhibit strong galaxy features, the lines seen, and the galaxy redshift. For reference, the table also lists the redshift determined by the nearby comparison method. In all cases, the redshifts found by the two methods agree within better than 0.01.

4. Discussion

4.1. Functional Model of SN Ia Lightcurve

To model our observed VR-band lightcurves, we choose the following function, $\phi(t)$, to describe the difference flux normalized to the difference flux at the time of maximum brightness in the VR-band:

$\phi = 0.0$ for $t < t_r$
$\phi = \frac{(t-t_r)^2}{t_r(t_r-n)}$ for $t_r < t < n$
$\phi = 1 - \frac{t^2}{nt_r}$ for $n < t < 0$
$\phi = 1 - \gamma t^2$ for $0 < t < m$
$\phi = 1 - m^2\gamma + 2m\gamma\tau(e^{\frac{m-t}{\tau}} - 1)$ for $t > m$

where t is the SN phase in rest-frame days scaled such that $t = 0$ is the time of maximum, ϕ is the ratio of observed VR-band flux at t to maximum flux, t_r is the time of explosion, n and m are arbitrary SN phases such that $n < 0$ and $m > 0$, γ is an arbitrary constant, and τ measures the decay time of the late-time lightcurve. The early-time portion of our model is motivated by Riess et al. (1999). Riess et al. fit their SN Ia lightcurves prior to -10 days with the expanding fireball model of Goldhaber et al. (1998) which has the functional form of a parabola with a minimum at the time of explosion. We model the expanding fireball as $\phi = \alpha(t - t_r)^2$. We choose an exponential for the late-time lightcurve shape because we expect the luminosity to be dominated by radioactive decay. For the exponential we pick the generic form $\phi = \phi_o e^{-\frac{t-t_m}{\tau}} + c$. The form of ϕ between $-n < t < 0$ and $0 < t < m$ is taken to be two arbitrary second degree polynomials constrained to be 1 at $t = 0$. We use the forms $\phi = 1 - \beta t^2$ and $\phi = 1 - \gamma t^2$ respectively. We leave n and m as free parameters in our fit. By requiring that ϕ be a smoothly connected function (i.e. that the value of ϕ and its first derivative are everywhere continous), we eliminate α, β, c, ϕ_o, and t_m. This results in the form of ϕ given above, with t_r, τ, n, m, and γ as the 5 remaining free parameters.

In the following sections, we will use this model to estimate the time, t_{max}, of observed frame maximum brightness, VR_{max}, for each SNe and to place constraints on the interval between the time-of-explosion and maximum brightness.

4.2. Estimation of t_{max}

For each SN presented, we determine t_{max} and VR_{max} using the functional SN Ia model presented in Section 4.1. We do so by adding t_{max} and VR_{max} as free parameters to the model such that

$f_{obs}(t_{obs}) = VR_{max}\phi(\frac{t_{obs}-t_{max}}{z})$

where f_{obs} is the observed flux, t_{obs} is the time of the observation, and z is the SN redshift.

Using the C-MINUIT implementation of the MINUIT[1] minimization package, we individually determine the best fit for each lightcurve to f_{obs} by minimizing χ^2. Table 1 gives the t_{max} and VR_{max} values for each SN along with the parabolic errors returned by the MIGRAD processor in MINUIT. We emphasize that these fits are performed on the lightcurves as observed with no K-corrections, reddening corrections, or adjustments to account for SN Ia lightcurve shape. We use these fits to obtain estimates of t_{max} and VR_{max} for each SN and not to assess whether our model, $\phi(t)$, provides a good description of the SN Ia lightcurve. We will discuss the validity of our model below in Section 4.3. For now we choose this model to estimate t_{max} and VR_{max} because we assume that the SN Ia lightcurve is a smooth, continuous function with single maximum and an asymmetric shape. $f_{obs}(t_{obs})$ provides a generic model for such a curve and should give a reasonable description of the maximum. To provide an initial assessment of this assumption we note that for each SN the best fit curve generally has a χ^2 value close to 1.

For each SN, we use our estimation of t_{max} and its measured redshift to determine the rest-frame phase, relative to t_{max}, of each observation. In the cases where a galaxy redshift is available (see Table 14), we use its value for the SN's redshift. Tables 2–12 give the phase and the significance (S/N) of each measurement. Table 1 lists the phase of the first S/N>5 observation for each SN.

We scale the difference fluxes to VR_{max} and correct for time dilation using the redshift determined in Section 3.2 to obtain the lightcurves shown in Figures 2–6. The SNe are presented grouped by redshift to minimize the impact of K-corrections. We expect the observed frame VR-band lightcurve to vary with redshift as the VR filter samples different portions of the rest-frame spectrum. Because the spectra of SNe Ia near the time of explosion are not well-studied and because we lack multi-epoch multi-band data for our lightcurves, we bin our data by redshift rather than apply K-corrections. We choose a bin size of 0.03 in

[1]See http://wwwasdoc.web.cern.ch/wwwasdoc/minuit/minmain.html for documentation on the MINUIT package.

redshift to maximize the number of SNe per bin while keeping the difference in K-corrections between redshifts within a bin small.

4.3. Construction of Composite of SN Ia Lightcurve

Using the normalized $\frac{f_{VR}}{VR_{max}}$ lightcurves presented in Section 4.2, we construct a composite SN Ia lightcurve that is well-sampled from the time of explosion to +60 days. We include SNe from the redshift bin z=0.135–0.165 to create the composite. For this redshift bin the center of our broadband filter corresponds to approximately 5200Å in the rest-frame, close to V-band. We would expect the light passing through this filter to be continuum-dominated, though some FeII & III, SiII, and SII features are present (Filippenko 1997). We use our composite lightcurve to examine the SN Ia lightcurve. In particular we discuss how well the functional form presented in Section 4.1 describes the lightcurve shape by performing a multi-parameter fit to the composite lightcurve. We also discuss the rise time to maximum brightness as parameterized by t_r in our functional model.

Using C-MINUIT to minimize χ^2, we perform a multi-parameter fit of $\phi(t)$ to the composite lightcurve, including only data between -30 rest-frame days and +60 rest-frame days so as not to allow the flat baseline to dominate the χ^2 of our best fit. Though we fit all four SNe simultaneously, we also refit for t_{max} and VR_{max} of each individual SN in the composite. For each SN, the best fit t_{max} obtained through the simulataneous fit agrees with the t_{max} found in the individual fits in Section 4.2 to within one observed-frame day. An initial fit to all four SNe in the z=0.135–0.165 bin indicates that SM-2004-LMC-1060 is a much faster decliner than the other SNe in the bin, a result that can be verified from a qualitative inspection of Figure 3. Removing this SN from the composite lightcurve, we refit $\phi(t)$ and find a best fit $\chi^2/d.o.f.$ of 1.16 for 38 $d.o.f.$. A summary of the parameters and their 1σ parabolic error uncertainties is given in Table 15.

From this fit we conclude that our functional model provides a reasonable description of the overall shape of the observed VR-band lightcurve for a SN Ia with z between 0.135 and 0.165. To draw further conclusions about the SN Ia lightcurve from the best fit parameters, we must discuss them in the context of the systematic effects that might alter the overall composite lightcurve shape and also of any effects introduced by using multiple SNe with different systematics to create the composite. We discuss the three largest systematic effects affecting our composite lightcurve: 1) the lack of K-corrections to account for SNe at different redshifts; 2) intrinsic diversity in the SN Ia family; and 3) reddening from the host galaxies, the LMC, and the Milky Way.

To examine the effects of the systematics, we create a tool to construct empirical models of observed VR-band lightcurves using a library of nearby SN Ia spectra and lightcurves. The lightcurve library spans a wide range of Δm_{15}[2] values (see Phillips, M. M. 1993) and the spectral library provides a typical SN Ia spectrum for each phase of the SN lightcurve from -10 to $+70$ rest-frame days (Nugent et al. 2002). We use these libraries to construct observed VR-band lightcurves with a specified redshift and Δm_{15} ranging from 0.8–1.9 as follows. By applying the Δm_{15} weighting method of Prieto et al. (2006), we first construct $BVRI$ lightcurves for the specified Δm_{15} value. We then "warp" the spectrum to match the expected, rest-frame $B-V$ color at each phase. Finally we convolve the transmission curve of the VR filter (see Figure 1) with the redshifted spectrum and obtain the observed VR-band flux for a given phase. We use a similar procedure to construct reddened lightcurves. After warping the library spectrum to match the expected color for the specified Δm_{15} value, we approximate the host galaxy reddening by applying the Cardelli et al. (1989) Galactic reddening law using $R_v = 3.1$ to the spectrum (see Riess et al. 1986b for discussion of host galaxy reddening laws). We then redshift the spectrum and apply the LMC reddening law of Fitzpatrick (1986) with $R_v = 3.3$. We also add the Galactic reddening using the Cardelli et al. law with $R_v = 3.1$. Finally, as in the unreddened case, we convolve the reddened, redshifted spectrum with the VR-band transmission filter to obtain the observed VR-band flux. As with our own data, we normalize these lightcurves to the flux at the time of maximum to create model $\frac{f_{VR}}{VR_{max}}$ lightcurves.

We use this tool in the following sections to help us understand the impact of systematic effects on our findings.

4.3.1. K-corrections

The general K-correction formula (Schmidt et al. 1998, and Nugent et al. 2002) is used to "correct" for the fact that, in a given filter, observations of SNe with different redshifts sample different portions of the SN Ia rest-frame spectrum. The observations are typically normalized to the filter most closely matching the portion of the rest-frame spectrum sampled by the filter in the observed frame. To apply such a correction to a given observation ideally requires a spectrum taken at the same phase as the observation. Because there are few high-quality SN Ia spectra prior to -10 rest-frame days, we choose not to K-correct our lightcurves. Instead, we choose SNe from a narrow range of redshifts to avoid introducing

[2]The value of Δm_{15} refers to the difference between the B-band SN brightness in magnitudes at maximum brightness and at $+15$ rest-frame days.

scatter into our composite by sampling very different portions of the SN Ia spectrum.

To estimate the variation between the SNe in our bin, we construct unreddened observed VR-band lightcurves at the redshifts of the SNe in our composite using the tool described above. We choose a fiducial Δm_{15} of 1.2 for these model lightcurves. Between -10 and $+80$ rest-frame days, the flux/maximum flux ratio of the three lightcurves differs by less than 3% with the maximum spread between the three at approximately +15 days. All three lightcurves reach maximum brightness at the same phase relative to rest-frame B-band maximum. On the rising portion, their $\frac{f_{VR}}{VR_{max}}$ lightcurves differ by less than 0.2%. These tests indicate that the systematic error contributed to an estimate of the time to maximum brightness using a composite lightcurve of SNe at redshifts between 0.135–0.165 without K-corrections is negligible.

In addition to minimizing scatter between SNe at different redshifts, K-corrections would provide a means for matching our observed VR-band lightcurves to standard bands in the rest-frame. At z=0.15, the central redshift of the SNe in our composite lightcurve, the observed VR-band most closely matches the rest-frame V-band. To compare the lightcurves of the observed VR-band at z=0.15 and V-band at z=0, we construct $\frac{f_{VR}}{VR_{max}}$ lightcurves between -10 and $+80$ rest-frame days with Δm_{15} of 1.2. Prior to maximum, the two lightcurves differ by $\sim$2% and reach maximum brightness at approximately the same phase relative to B-band maximum. Their times of maximum differ by less than the resolution of our model lightcurves which is $\sim$0.5 rest-frame days. Using a cubic spline fit to the lightcurves near maximum, we find the difference in the times of maximum to be 1.1 rest-frame days. Post-maximum, the lightcurves diverge with the observed VR-band lightcurve declining more rapidly. From this comparison we conclude that for the rising portion of the lightcurve, the observed VR-band lightcurve–with the time axis shifted to the rest-frame–is a close approximation of the rest-frame V-band lightcurve. The systematic error in an estimate of the time to V-band maximum using the observed VR-band lightcurve will be less than $\pm$1.1 rest-frame days.

4.3.2. SN Ia Diversity

Intrinsic diversity in the SN Ia family will also impact our estimate of the time-to-maximum from our composite lightcurve. To reduce the most gross impact of this effect, we remove the obvious fast riser and decliner SM-2004-LMC-1060 from our composite lightcurve.

To account for the effect of variation between the remaining SNe, we add a free "stretch" parameter, s, for each of the SNe in the fit following Goldhaber et al. (2001). Using C-

MINUIT we perform a multi-parameter fit to the composite lightcurve and fix the stretch parameter for one of the SNe in the composite to 1, no stretch. Effectively, the other SNe in the composite are normalized to the shape of the unstretched SN. We choose SM-2004-LMC-944 as our fiducial SNe, because it has the median width of the 3 SNe in the composite. We present the results of this fit in Table 15. We characterize the "shape" of our best fit by the value of Δm_{-10}, the difference in magnitudes between the VR-band flux at -10 rest-frames days and at maximum. For the best fit normalized to the shape of SM-2004-LMC-944, Δm_{-10} is 0.52 and the time-to-maximum is 19.2±1.3 rest-frame days. Figure 18 shows the best fit with the composite lightcurve. The phases of the data points have been stretched according to the values of s returned by the best fit. By scaling the time-to-maximum by the best-fit stretch parameters for each of the other SNe in the composite, we can determine the time-to-maximum for different values of Δm_{-10}. For SM-2004-LMC-803 which has a Δm_{-10} of 0.53, the time-to-maximum is 18.96 rest-frame days. For SM-2004-LMC-797 with a Δm_{-10} of 0.39, the time-to-maximum is 20.93 rest-frame days.

Our fits indicate that, like the declining portion of the lightcurve, the shape of the rising lightcurve of a SN Ia differs between individual SNe in a way that can be paramaterized by a stretch factor. With our current data, however, we cannot compare these rising lightcurve shape parameters with those describing the decline rate. Our lightcurves are not reddening corrected and, as discussed below, the impact of reddening is most severe on the declining portion of our lightcurves. Without reddening corrections we cannot meaningfully compare the rate of rise with the rate of decline in our lightcurves. Further, because our VR-band lightcurve differs most significantly from the standard, V-band filter on the decline, comparing our findings to previous work in standard passbands is also difficult.

4.3.3. Reddening

Reddening from dust along the line-of-sight to the SNe also alters the shape of our composite lightcurve and impacts our estimates of the parameters in our functional SN Ia model, including the time-to-maximum. Because the SN spectrum evolves, the effect of reddening changes with SN phase. The bluer the intrinsic SN light, the larger the change in the observed color caused by dust along the line-of-sight. The light from the SNe in our sample is reddened by dust in three different locations: the host galaxy, the LMC, and the Galaxy. The line-of-sight dust introduces two different effects into our composite lightcurve: 1) the overall change in the shape of the composite lightcurve due to reddening and 2) increased scatter in the composite lightcurve due to differences in the line-of-sight reddening to the three separate SNe in the composite.

To examine the overall impact of reddening, we use the tool described above to create an unreddened $\frac{f_{VR}}{VR_{max}}$ lightcurve with $\Delta m_{15} = 1.2$ at a redshift of 0.15. We then create reddened lightcurves. For the host galaxy reddening we refer to the distribution of color excesses found by the ESSENCE survey (Wood-Vasey, private communication). Assuming $R_v = 3.1$, ESSENCE finds a mean value for $E(B-V)$ of 0.06. To obtain a reasonable estimate of $E(B-V)$ through the LMC, we double the mean value of the Galaxy-corrected $E(B-V)$ for LMC stars found by Harris et al. (1997) and use $E(B-V)$=0.26±0.055. We also use $E(B-V)$=0.07±0.01 through the Galaxy toward the LMC as suggested by Harris et al. who use the Oestreicher et al. (1995) SN1987A foreground reddening value. We find the ratio of the reddened model lightcurve flux to the unreddened model lightcurve flux at each phase, and multiply this ratio by the data point in our composite lightcurve at the corresponding phase. For data points prior to −10 days, we use the ratio at −10 days. In this way we effectively "redden" our composite lightcurve. We find that in our VR-band at z=0.15, the impact of reddening is significantly more severe on the declining arm of the lightcurve. The maximum change in $\frac{f_{VR}}{VR_{max}}$ due to reddening on the rising arm is ∼0.2%, while the maximum change on the declining arm is ∼5%. To get a more extreme estimate of the impact of reddening, we also create a reddened lightcurve with a host galaxy $E(B-V)$ of 0.25. This value represents approximately the 90th percentile host galaxy color excess found by the ESSENCE survey. Increasing the host galaxy reddening to this amount can change the $\frac{f_{VR}}{VR_{max}}$ lightcurve by up to ∼0.5% on the rising arm and ∼10% on the declining arm. Because the rising arm of the lightcurve is so much less susceptible to changes caused by reddening, we focus our analysis on the rising portion of our composite lightcurve and the constraints we can place on the time-to-maximum.

To understand how reddening impacts the value in the best fit of the parameter t_r, we refit the reddened composite to our functional model choosing SM-2004-LMC-944 as the fiducial SN for normalizing the stretch. We find that the estimate of the time-to-maximum, $-t_r$, is increased by 1.6 rest-frame days. From this we conclude that the systematic uncertainty in the time-to-maximum caused by reddening is approximately −1.6 rest-frame days. To examine whether the overall effect of reddening is always to increase the time-to-maximum, we choose extreme values for the color excess in the LMC, $E(B-V)$=1.26, and the Galaxy, $E(B-V)$=1.07 and refit the "reddened" composite lightcurve. As expected, the estimate of the time-to-maximum is more significantly altered; the absolute value of t_r increases by almost 2 rest-frame days. Notably, however, the reddening only increases, and never decreases, the estimate of the time-to-maximum. From this we conclude that the overall potential impact of reddening is to increase our estimate of the time-to-maximum by ∼1.6 rest-frame days assuming reasonable values of the color excess due to reddening. We modify the value of our time-to-maximum to reflect the impact of the reddening to obtain a

best estimate of 19.2±1.3−1.6*(red.)* rest-frame days.

We use Monte Carlo simulations to examine how the uncertainties in the LMC, Galaxy, and host galaxy reddenings as well as the differences between host galaxy reddening for each of the SNe impact our estimate of the overall effect of reddening. For each simulation, we create multiple realizations of a reddened composite lightcurve in the manner described above. We perform a multi-parameter fit on each realization and calculate the robust mean value of the time-to-maximum and its standard deviation. To isolate the effect of the uncertainty in each source of reddening, we hold the color excess values of the other reddening sources fixed and vary the source of interest. For example, to understand how the uncertainty in the LMC's color excess affects our estimate of the impact of reddening, we set the Galaxy's $E(B-V)$ to 0.07 and the host galaxy $E(B-V)$ for all three SNe to 0.06. For each realization, we draw the LMC's color excess from a gaussian distribution with a mean of 0.26 and a σ of 0.55, reflecting the values determined by Harris et al. We perform a similar Monte Carlo holding the LMC and host galaxy reddenings fixed while choosing the Galactic color excess from a gaussian distribution centered at 0.07 with a σ of 0.01. Finally, we estimate the combined impact of our uncertainty in the host galaxy reddening values and the differences between them for each SNe. Holding the LMC and Galactic reddening fixed in each realization, we choose a different host galaxy color excess for each SN from a distribution of host galaxy $E(B-V)$ similar to that found by the ESSENCE survey.

For each of the simulations described above, the 3σ-clipped mean value of the time-to-maximum matched that obtained by using the "best guess" values of the reddenings. The standard deviations about this mean provides an estimate of the systematic uncertainty in our reddening-corrected time-to-maximum caused by uncertainties in the reddening caused by each source. For the LMC, the standard deviation of the time-to-maximum is 0.014. For the Galaxy the standard deviation is 0.012. For the host galaxy reddenings the standard deviation is 0.067. Summing these numbers in quadrature, we arrive at an estimate of the total systematic uncertainty in the time-to-maximum due to reddening, ±0.07 rest-frame days.

4.4. Comparison with Previous Findings

Our investigation of systematic effects impacting our composite lightcurve yields the following conclusions. The lack of K-corrections on our SNe chosen from the narrow redshift range of 0.135–0.165 will have a negligible effect on the overall shape of our composite lightcurve. Without K-corrections, however, we must be careful in how we compare our observed VR-band lightcurve with the most closely matched rest-frame filter, the V-band.

We find that the rising portion of our observed VR-band lightcurve is similar to the rest-frame V-band, and that an estimate of the time-of-maximum from our composite lightcurve will differ from the V-band time-of-maximum by less than 1.1 rest-frame days. To account for intrinsic variability we introduce a stretch parameter for each of the SNe in the composite lightcurve and normalize the shape to SM-2004-LMC-944. We estimate that the overall effect of reddening on the time-to-maximum is to increase it by 1.6 rest-frame days. The systematic error in our estimate of the effect of reddening is ± 0.07 rest-frame days.

Based on the fits described above, the best fit parameters to our functional model give a time-of-explosion $19.2 \pm 1.3 - 1.6 \pm 0.07$ *(red.)* rest-frame days before maximum VR-band brightness for a SN Ia with a Δm_{-10} of 0.52. At a z of 0.15, we expect the observed VR-band to most closely match the rest-frame V-band lightcurve, and we add an additional systematic uncertainty of ± 1.1 rest-frame days to our estimate of the time-to-maximum in the V-band. Our findings give a smaller value for the time-to-maximum than that of Riess et al. (1999) for the fiducial V-band who find a time-to-maximum of 21.1 ± 0.2 days. The significance of this discrepancy is unclear. Our value for the time-to-maximum is normalized to an SN with VR-band $\Delta m_{-10} = 0.52$. As described above, comparing our values of Δm_{-10} with previous work is difficult. For this paper we note the discrepency but without a study that analyzes both our lightcurves and previous data in the same way, we cannot comment on its significance.

5. Conclusion

We present VR-band lightcurves and optical spectra of 11 SNe Ia behind the LMC discovered by the SuperMACHO survey[3]. Our data include some of the earliest pre-maximum detections of SNe Ia. We provide a functional model for the observed VR-band lightcurve from the time of explosion to +60 days by fitting a composite lightcurve to three SNe in the redshift bin of z=0.135–0.165. The data are fitted without K-corrections or reddening corrections; however, the set of SNe have been chosen to minimize the impact of these effects. Our function uses the expanding fireball model of Goldhaber et al. (1998) to describe the lightcurve immediately following the explosion. The best fit of our functional model to our composite, observed VR-band lightcurve gives a time-to-maximum of $19.2 \pm 1.3^{+0.0}_{-2.1}$ rest-frame days for a SN Ia with a Δm_{-10} of 0.52. Our simulations indicate that the VR-band time-of-maximum at z=0.15 should match the rest-frame V-band time-of-maximum to within 1.1 rest-frame days.

[3]See http://ctiokw.ctio.noao.edu/supermacho/SNrise for electronic data tables

We present this data to be used to test competing models of the SN Ia explosion mechanism by placing observational limits on the time to maximum and the shape of the rising lightcurve. Analyses of our data are limited by its being in a single band. While our broadband filter enables us to detect flux earlier, we cannot calibrate our lightcurves against the nearby sets of SNe Ia observed in $BVRI$.[4] An ideal study should include both a broadband filter and the standard filter set.

6. Acknowledgments

The SuperMACHO survey is being undertaken under the auspices of the NOAO Survey Program. We are very grateful for the support provided to the Survey program from the NOAO and the National Science Foundation. We are particularly indebted to the scientists and staff at the Cerro Tololo Interamerican Observatory for their assistance in helping us carry out the SuperMACHO survey. We also appreciate the invaluable help of Mr. Chance Reschke in building and maintaining the computing cluster we use for image analysis. SuperMACHO is supported by the STScI grant GO-10583. This project works closely with members of the ESSENCE supernova survey, and we are grateful for their input and assistance. The spectroscopic observations presented in this paper were obtained on the Magellan telescopes operated by the Las Campanas Observatory. We are grateful to the scientists and staff of LCO. Discussions with P. Pinto were invaluable in helping us understand the physics underlying our observations. We are also grateful to T. Matheson and M. Modjaz for their help with spectral identifications. The support of the McDonnell Foundation, through a Centennial Fellowship awarded to C. Stubbs, has been essential to the SuperMACHO survey. We are most grateful for the Foundation's support for this project. C. Stubbs and AG are also grateful for support from Harvard University. KHC's, MEH's, and SN's work was performed under the auspices of the U.S. Department of Energy, National Nuclear Security Administration by the University of California, Lawrence Livermore National Laboratory under contract No. W-7405-Eng-48. JLP's work is supported by STScI grant GO-9860.07. AC acknowledges the support of CONICYT (Chile) through FONDECYT grant 1051061. DM and LM acknowledge support from the Fondap Center for Astrophysics grant 15010003. DLW acknowledges financial support in the form of a Discovery Grant from the Natural Sciences and Engineering Research Council of Canada (NSERC).

[4]Because the transmission curve of our VR filter differs from the sum of the V-band and R-band transmissions, we cannot simply add the nearby V and R templates to obtain a VR template.

REFERENCES

Ajhar, E. A., Tonry, J. L., Blakeslee, J. P., Riess, A. G., & Schmidt, B. P. 2001, ApJ, 559, 584

Alard, C., & Lupton, R. H. 1998, ApJ, 503, 325

Alard, C. 2000, A&AS, 144, 363

Alcock, C., et al. 1999, ApJ, 521, 602

Alcock, C., et al. 2000, ApJ, 542, 281

Aldering, G., Knop, R., & Nugent, P. 2000, AJ, 119, 2110

Allington-Smith, J., et al. 1994, PASP, 106, 983

Astier, P., et al. 2006, A&A (in press)

Barris, B. J., Tonry, J. L., Novicki, M. C., & Wood-Vasey, W. M. 2005, AJ, 130, 2272

Bigelow, B. C., Dressler, A. M., Shectman, S. A., & Epps, H. W. 1998, Proc. SPIE, 3355, 225

Bigelow, B. C., & Dressler, A. M. 2003, Proc. SPIE, 4841, 1727

Cardelli, J. A., Clayton, G. C., & Mathis, J. S. 1989, ApJ, 345, 245

Filippenko, A. V. 1997, ARA&A, 35, 309

Gibson, B. K., et al. 2000, ApJ, 529, 723

Gössl, C. A., & Riffeser, A. 2002, A&A, 381, 1095

Goldhaber, G., & Supernova Cosmology Project Collaboration 1998, Bulletin of the American Astronomical Society, 30, 1325

Goldhaber, G., et al. 2001, ApJ, 558, 359

Hamuy, M., Phillips, M. M., Suntzeff, N. B., Schommer, R. A., Maza, J., & Aviles, R. 1996, AJ, 112, 2391

Hamuy, M., Phillips, M. M., Suntzeff, N. B., Schommer, R. A., Maza, J., Smith, R. C., Lira, P., & Aviles, R. 1996, AJ, 112, 2438

Hamuy, M., Phillips, M. M., Wells, L. A., & Maza, J. 1993, PASP, 105, 787

Harris, J., Zaritsky, D., & Thompson, I. 1997, AJ, 114, 1933

Kim, A., Goobar, A., & Perlmutter, S. 1996, PASP, 108, 190

Kowalski, M., et al. 2004, American Astronomical Society Meeting Abstracts, 205

Lupton, R., & Monger, P. 1991, Unpublished paper, 1991,

Matheson, T., et al. 2005, AJ, 129, 2352

Miknaitis, G., et al. 2005, American Astronomical Society Meeting Abstracts, 206

Nugent, P., Kim, A., & Perlmutter, S. 2002, PASP, 114, 803

Oestreicher, M. O., Gochermann, J., & Schmidt-Kaler, T. 1995, A&AS, 112, 495

Perlmutter, S., et al. 1999, ApJ, 517, 565

Phillips, M. M. 1993, ApJ, 413, L105

Poznanski, D., Gal-Yam, A., Maoz, D., Filippenko, A. V., Leonard, D. C., & Matheson, T. 2002, PASP, 114, 833

Prieto, J. L., Rest, A., & Suntzeff, N. B. 2006, ArXiv Astrophysics e-prints, arXiv:astro-ph/0603407

Rest, A., et al. 2005, ApJ, 634, 1103

Riess, A. G., Press, W. H., & Kirshner, R. P. 1995, ApJ, 438, L17

Riess, A. G., Press, W. H., & Kirshner, R. P. 1996, ApJ, 473, 88

Riess, A. G., Press, W. H., & Kirshner, R. P. 1996, ApJ, 473, 588

Riess, A. G., et al. 1998, AJ, 116, 1009

Riess, A. G., et al. 1999, AJ, 118, 2675

Schlegel, D. J., Finkbeiner, D. P., & Davis, M. 1998, ApJ, 500, 525

Schmidt, B. P., et al. 1998, ApJ, 507, 46

Stubbs, C. W., et al. 2002, Bulletin of the American Astronomical Society, 34, 1232

Suntzeff, N. B., et al. 1999, AJ, 117, 1175

van Dokkum, P. G. 2001, PASP, 113, 1420

Zaritsky, D., Harris, J., Thompson, I. B., & Grebel, E. K. 2004, AJ, 128, 1606

Table 1. SuperMACHO Supernovae 2004

SN ID	RA (J2000)	DEC	z	galaxy z	phase$_{S/N>5}$	$t_{max}(MJD)$	VR_{max}	phase$_{f=0}$
SM-2004-LMC-64[a]	04:55:22.266	-67:30:44.31	0.22	···	-7.9	53292.97±0.86	64.93±1.04	-29.3
SM-2004-LMC-772	05:19:42.656	-67:31:35.83	0.19	···	-18.0	53316.74±0.39	79.83±1.13	-566.8
SM-2004-LMC-797	05:59:13.224	-71:49:59.27	0.145	···	-17.2	53318.94±1.00	96.05±1.42	-20.7
SM-2004-LMC-803	05:47:05.071	-71:46:28.36	0.16	···	-10.4	53327.46±0.53	69.86±0.87	-27.8
SM-2004-LMC-811	04:56:31.608	-66:58:09.21	0.27	···	-7.6	53324.87±0.97	31.12±0.62	-20.2
SM-2004-LMC-917	05:21:19.819	-70:51:12.57	0.11	···	-5.5	53350.52±0.28	198.76±0.56	-24.6
SM-2004-LMC-944	05:11:48.947	-70:29:38.66	0.15	···	-12.7	53358.87±0.50	60.49±0.49	-37.9
SM-2004-LMC-1002	04:53:09.337	-69:41:00.13	0.35	0.350	-8.8	53356.12±15.44	14.93±3.24	-18.3
SM-2004-LMC-1052	06:01:36.188	-71:59:29.88	0.34	0.348	-9.5	53361.10±2.81	17.09±0.84	-22.2
SM-2004-LMC-1060	05:35:30.148	-71:06:34.05	0.16	0.154	-13.5	53363.94±1.96	76.73±3.60	-326.4
SM-2004-LMC-1102	05:37:13.676	-68:50:00.93	0.22	···	-13.1	53364.30±1.22	31.65±1.17	-27.0

[a]SM-LMC-2004-64 also has IAU designation SN2004gb.

Note. — Summary of SNe Ia presented in this paper. *SN ID* gives the SuperMACHO survey identification of each SN. z is the redshift of the SN determined by comparing its spectrum to a nearby SN. *Galaxy z* is the redshift of the SN's host galaxy determined, when possible, from galaxy features in the spectrum. $phase_{S/N>5}$ indicates the rest-frame phase in days at which the first detection with S/N > 5 was made. t_{max} is the time of VR-band maximum, VR_{max}. Both t_{max} and VR_{max} are given with their 1σ uncertainties. VR_{max} is in flux units normalized to a zeropoint of 25. $phase_{f=0}$ gives the rest-frame phase of the last zero flux measurement prior to the SN's detection.

Table 2. Lightcurve for SM-2004-LMC-64

MJD	Rest Phase	Diff flux	flux err	$\frac{f_{VR}}{VR_{max}}$	$\frac{f_{VR}}{VR_{max}}$ err	S/N
53257.27	-29.3	-0.410	1.168	-0.006	2.852	0.35
53266.23	-21.9	-3.083	2.099	-0.047	0.681	1.47
53283.31	-7.9	40.694	2.666	0.627	0.067	15.26
53287.37	-4.6	54.304	5.662	0.836	0.105	9.59
53289.30	-3.0	60.166	1.196	0.927	0.026	50.31
53291.20	-1.4	66.107	1.746	1.018	0.031	37.86
53293.18	0.2	68.740	2.673	1.059	0.042	25.71
53297.30	3.5	60.655	1.158	0.934	0.025	52.37
53299.19	5.1	58.575	1.269	0.902	0.027	46.15
53301.18	6.7	53.818	1.580	0.829	0.033	34.06
53321.21	23.1	20.107	1.633	0.310	0.083	12.31
53325.29	26.5	16.623	1.055	0.256	0.065	15.76
53327.33	28.2	16.610	0.894	0.256	0.056	18.58
53331.32	31.4	12.894	0.930	0.199	0.074	13.87
53344.29	42.1	7.851	0.834	0.121	0.107	9.41
53348.36	45.4	7.481	2.565	0.115	0.343	2.92
53350.20	46.9	6.244	0.692	0.096	0.112	9.02
53352.31	48.6	9.055	2.524	0.139	0.279	3.59
53354.26	50.2	6.311	0.891	0.097	0.142	7.08
53356.26	51.9	6.288	0.849	0.097	0.136	7.41

Note. — Difference flux lightcurve for SM-2004-LMC-64. Rest Phase is given in rest-frame days relative to observed VR-band maximum. *Diff flux* is the observed VR-band difference flux at the position of the SN given in Table 1. These fluxes are determined using the N(N-1)/2 method of Barris et al. (2005) and are normalized to a zeropoint of 25. *Flux err* is the error in *Diff flux*. $\frac{f_{VR}}{VR_{max}}$ is the difference flux normalized by the maxixmum VR-band flux, VR_{max}, given in Table 1. $\frac{f_{VR}}{VR_{max}}$ err is the error in $\frac{f_{VR}}{VR_{max}}$ and includes the uncertainty in VR_{max}. *S/N* gives the significance of the difference flux measurement.

Table 3. Lightcurve for SM-2004-LMC-772

MJD	Rest Phase	Diff flux	flux err	$\frac{f_{VR}}{VR_{max}}$	$\frac{f_{VR}}{VR_{max}}$ err	S/N
53257.37	-49.9	1.176	0.995	0.015	0.846	1.18
53289.35	-23.0	1.866	1.074	0.023	0.576	1.74
53295.28	-18.0	7.319	0.994	0.092	0.137	7.36
53315.30	-1.2	78.786	1.445	0.987	0.023	54.52
53323.27	5.5	64.686	1.135	0.810	0.023	56.99
53327.35	8.9	52.777	1.238	0.661	0.027	42.61
53329.36	10.6	48.186	1.250	0.604	0.030	38.56
53344.35	23.2	25.464	1.204	0.319	0.049	21.16
53346.34	24.9	22.006	1.346	0.276	0.063	16.35
53348.24	26.5	21.588	0.850	0.270	0.042	25.40
53350.29	28.2	20.707	1.089	0.259	0.054	19.02
53352.22	29.8	18.823	1.145	0.236	0.062	16.44
53354.22	31.5	17.099	1.136	0.214	0.068	15.05
53356.24	33.2	16.935	0.655	0.212	0.041	25.86
53358.32	34.9	14.938	0.910	0.187	0.063	16.41
53360.28	36.6	13.548	0.710	0.170	0.054	19.08
53379.13	52.4	8.437	0.733	0.106	0.088	11.51
53381.15	54.1	7.082	0.762	0.089	0.109	9.29
53383.15	55.8	7.653	0.600	0.096	0.080	12.75
53387.13	59.2	7.282	1.002	0.091	0.138	7.27

Note. — Difference flux lightcurve for SM-2004-LMC-772. See Table 2 for explanation of column headings.

Table 4. Lightcurve for SM-2004-LMC-797

MJD	Rest Phase	Diff flux	flux err	$\frac{f_{VR}}{VR_{max}}$	$\frac{f_{VR}}{VR_{max}}$ err	S/N
53287.28	-27.7	7.218	13.565	0.075	1.879	0.53
53295.24	-20.7	-0.123	0.930	-0.001	7.533	0.13
53297.19	-19.0	1.495	0.946	0.016	0.633	1.58
53299.27	-17.2	10.651	0.770	0.111	0.074	13.82
53315.20	-3.3	90.763	1.869	0.945	0.025	48.56
53323.21	3.7	94.325	1.822	0.982	0.024	51.78
53325.30	5.6	89.474	1.775	0.932	0.025	50.41
53327.36	7.4	85.997	2.309	0.895	0.031	37.24
53344.28	22.1	36.229	1.096	0.377	0.034	33.06
53348.31	25.7	31.168	0.843	0.324	0.031	36.99
53354.26	30.9	23.170	1.838	0.241	0.081	12.60
53356.28	32.6	22.785	0.817	0.237	0.039	27.90
53358.34	34.4	20.772	1.042	0.216	0.052	19.94
53360.30	36.1	18.483	0.768	0.192	0.044	24.06
53379.13	52.6	13.162	0.969	0.137	0.075	13.58
53381.15	54.3	11.145	0.942	0.116	0.086	11.83
53383.15	56.1	9.917	0.684	0.103	0.071	14.50
53387.12	59.5	10.317	0.966	0.107	0.095	10.69

Note. — Difference flux lightcurve for SM-2004-LMC-797. See Table 2 for explanation of column headings.

Table 5. Lightcurve for SM-2004-LMC-803

MJD	Rest Phase	Diff flux	flux err	$\frac{f_{VR}}{VR_{max}}$	$\frac{f_{VR}}{VR_{max}}$ err	S/N
53295.23	-27.8	0.361	1.092	0.005	3.029	0.33
53297.18	-26.1	-0.886	1.037	-0.013	1.170	0.85
53315.34	-10.4	35.393	1.081	0.507	0.033	32.74
53323.21	-3.7	64.359	1.536	0.921	0.027	41.91
53325.30	-1.9	69.728	1.529	0.998	0.025	45.60
53327.23	-0.2	69.143	1.636	0.990	0.027	42.26
53331.30	3.3	65.585	1.389	0.939	0.025	47.21
53346.37	16.3	31.534	7.572	0.451	0.240	4.16
53348.27	17.9	29.872	0.814	0.428	0.030	36.72
53354.27	23.1	26.101	2.085	0.374	0.081	12.52
53356.28	24.8	21.420	0.823	0.307	0.040	26.02
53358.33	26.6	19.618	1.053	0.281	0.055	18.62
53360.25	28.3	18.968	0.820	0.272	0.045	23.12
53377.14	42.8	9.255	0.696	0.132	0.076	13.29
53381.12	46.3	7.939	0.971	0.114	0.123	8.18
53383.12	48.0	8.478	0.661	0.121	0.079	12.82
53387.15	51.5	8.239	0.985	0.118	0.120	8.37

Note. — Difference flux lightcurve for SM-2004-LMC-803. See Table 2 for explanation of column headings.

Table 6. Lightcurve for SM-2004-LMC-811

MJD	Rest Phase	Diff flux	flux err	$\frac{f_{VR}}{VR_{max}}$	$\frac{f_{VR}}{VR_{max}}$ err	S/N
53287.37	-29.5	17.718	14.242	0.569	0.804	1.24
53289.31	-28.0	-1.034	0.705	-0.033	0.682	1.47
53295.19	-23.4	0.212	0.779	0.007	3.681	0.27
53297.30	-21.7	-0.317	0.795	-0.010	2.507	0.40
53299.19	-20.2	0.174	0.830	0.006	4.763	0.21
53301.18	-18.7	-1.227	1.016	-0.039	0.828	1.21
53315.25	-7.6	23.727	1.111	0.762	0.051	21.36
53321.21	-2.9	31.035	3.161	0.997	0.104	9.82
53325.29	0.3	31.162	1.091	1.001	0.040	28.55
53327.33	1.9	30.392	1.117	0.977	0.042	27.21
53331.32	5.1	30.126	1.164	0.968	0.044	25.88
53344.29	15.3	18.166	1.125	0.584	0.065	16.15
53348.36	18.5	7.853	2.961	0.252	0.378	2.65
53350.20	19.9	12.294	0.695	0.395	0.060	17.68
53352.31	21.6	10.440	1.105	0.335	0.108	9.45
53354.17	23.1	9.706	0.986	0.312	0.103	9.85
53360.35	27.9	6.264	0.976	0.201	0.157	6.42
53385.14	47.5	3.283	0.671	0.105	0.205	4.89
53387.14	49.0	3.416	0.886	0.110	0.260	3.85

Note. — Difference flux lightcurve for SM-2004-LMC-811. See Table 2 for explanation of column headings.

Table 7. Lightcurve for SM-2004-LMC-917

MJD	Rest Phase	Diff flux	flux err	$\frac{f_{VR}}{VR_{max}}$	$\frac{f_{VR}}{VR_{max}}$ err	S/N
53295.27	-49.8	0.075	0.588	0.000	7.801	0.13
53297.22	-48.0	1.027	0.673	0.005	0.655	1.53
53301.24	-44.4	0.584	1.077	0.003	1.844	0.54
53315.22	-31.8	-0.731	0.660	-0.004	0.903	1.11
53323.20	-24.6	0.248	0.503	0.001	2.027	0.49
53325.36	-22.7	0.880	1.209	0.004	1.374	0.73
53329.29	-19.1	-0.947	0.626	-0.005	0.661	1.51
53331.33	-17.3	3.916	0.790	0.020	0.202	4.96
53344.36	-5.6	163.411	2.276	0.822	0.014	71.79
53346.35	-3.8	181.941	2.037	0.915	0.012	89.34
53348.19	-2.1	192.288	1.344	0.967	0.008	143.09
53350.27	-0.2	199.294	0.684	1.003	0.004	291.32
53352.33	1.6	195.035	1.130	0.981	0.006	172.60
53360.35	8.9	153.213	2.068	0.771	0.014	74.08
53385.17	31.2	53.737	1.428	0.270	0.027	37.64

Note. — Difference flux lightcurve for SM-2004-LMC-917. See Table 2 for explanation of column headings.

Table 8. Lightcurve for SM-2004-LMC-944

MJD	Rest Phase	Diff flux	flux err	$\frac{f_{VR}}{VR_{max}}$	$\frac{f_{VR}}{VR_{max}}$ err	S/N
53315.26	-37.9	0.070	0.778	0.001	11.177	0.09
53323.34	-30.9	0.609	0.898	0.010	1.475	0.68
53327.22	-27.5	-0.557	0.851	-0.009	1.528	0.65
53329.27	-25.7	-0.563	0.689	-0.009	1.222	0.82
53331.23	-24.0	2.834	1.696	0.047	0.598	1.67
53342.24	-14.5	10.673	2.345	0.176	0.220	4.55
53344.24	-12.7	20.172	0.552	0.333	0.029	36.53
53346.32	-10.9	29.423	0.661	0.486	0.024	44.53
53348.35	-9.1	38.566	0.635	0.638	0.018	60.72
53350.24	-7.5	46.252	0.739	0.765	0.018	62.60
53356.33	-2.2	59.033	0.557	0.976	0.012	105.97
53358.18	-0.6	60.552	0.768	1.001	0.015	78.88
53360.32	1.3	59.972	1.167	0.991	0.021	51.38
53381.12	19.3	25.134	0.623	0.416	0.026	40.36
53383.12	21.1	23.555	0.521	0.389	0.024	45.17
53387.15	24.6	18.505	0.621	0.306	0.035	29.81

Note. — Difference flux lightcurve for SM-2004-LMC-944. See Table 2 for explanation of column headings.

Table 9. Lightcurve for SM-2004-LMC-1002

MJD	Rest Phase	Diff flux	flux err	$\frac{f_{VR}}{VR_{max}}$	$\frac{f_{VR}}{VR_{max}}$ err	S/N
53295.18	-45.1	-0.021	0.828	-0.001	40.005	0.02
53297.30	-43.6	-0.590	0.738	-0.040	1.269	0.80
53299.19	-42.2	-1.349	1.676	-0.090	1.261	0.80
53301.17	-40.7	-1.034	1.109	-0.069	1.095	0.93
53315.24	-30.3	0.282	0.822	0.019	2.922	0.34
53325.28	-22.8	0.576	0.746	0.039	1.312	0.77
53327.32	-21.3	-1.888	0.747	-0.126	0.451	2.53
53329.34	-19.8	-0.643	0.541	-0.043	0.868	1.19
53331.35	-18.3	-0.582	1.241	-0.039	2.144	0.47
53344.31	-8.7	9.045	1.217	0.606	0.256	7.43
53346.28	-7.3	13.110	1.145	0.878	0.234	11.45
53348.22	-5.9	12.412	0.646	0.831	0.223	19.22
53350.19	-4.4	13.807	0.676	0.925	0.223	20.44
53352.26	-2.9	13.994	0.736	0.937	0.224	19.01
53354.18	-1.4	15.154	0.914	1.015	0.225	16.59
53360.37	3.1	11.610	3.738	0.778	0.388	3.11
53385.14	21.5	2.049	0.674	0.137	0.394	3.04

Note. — Difference flux lightcurve for SM-2004-LMC-1002. See Table 2 for explanation of column headings.

Table 10. Lightcurve for SM-2004-LMC-1052

MJD	Rest Phase	Diff flux	flux err	$\frac{f_{VR}}{VR_{max}}$	$\frac{f_{VR}}{VR_{max}}$ err	S/N
53295.24	-49.2	-0.666	0.843	-0.039	1.265	0.79
53297.19	-47.7	0.583	0.952	0.034	1.634	0.61
53299.27	-46.1	0.859	0.752	0.050	0.876	1.14
53315.20	-34.3	1.078	1.180	0.063	1.096	0.91
53323.21	-28.3	2.211	0.847	0.129	0.386	2.61
53325.30	-26.7	0.144	0.838	0.008	5.810	0.17
53327.36	-25.2	0.578	1.357	0.034	2.348	0.43
53331.30	-22.2	-0.349	1.339	-0.020	3.836	0.26
53344.28	-12.6	3.058	0.867	0.179	0.288	3.53
53348.31	-9.5	8.714	0.673	0.510	0.092	12.95
53352.34	-6.5	10.739	1.842	0.628	0.179	5.83
53354.26	-5.1	16.207	1.952	0.948	0.130	8.30
53356.28	-3.6	16.779	0.984	0.982	0.077	17.05
53358.34	-2.1	16.838	0.954	0.985	0.075	17.65
53360.30	-0.6	16.303	0.907	0.954	0.074	17.98
53379.13	13.5	7.213	0.908	0.422	0.135	7.95
53381.15	15.0	5.784	1.104	0.338	0.197	5.24
53383.15	16.5	4.348	0.750	0.254	0.179	5.80
53387.12	19.4	2.766	1.148	0.162	0.418	2.41

Note. — Difference flux lightcurve for SM-2004-LMC-1052. See Table 2 for explanation of column headings.

Table 11. Lightcurve for SM-2004-LMC-1060

MJD	Rest Phase	Diff flux	flux err	$\frac{f_{VR}}{VR_{max}}$	$\frac{f_{VR}}{VR_{max}}$ err	S/N
53315.33	-41.9	0.562	0.843	0.007	1.501	0.67
53323.23	-35.1	0.544	0.709	0.007	1.303	0.77
53325.33	-33.3	1.628	0.759	0.021	0.469	2.14
53329.32	-29.8	1.489	0.940	0.019	0.633	1.58
53344.32	-16.9	3.832	1.381	0.050	0.364	2.77
53348.32	-13.5	12.766	0.782	0.166	0.077	16.33
53350.33	-11.7	24.416	1.230	0.318	0.069	19.85
53356.29	-6.6	57.413	0.979	0.748	0.050	58.64
53358.25	-4.9	65.401	1.287	0.852	0.051	50.81
53360.25	-3.2	73.437	1.385	0.957	0.051	53.01
53377.15	11.4	44.074	0.901	0.574	0.051	48.90
53381.13	14.8	36.533	1.243	0.476	0.058	29.39
53383.13	16.5	32.523	0.863	0.424	0.054	37.68
53387.16	20.0	24.534	0.980	0.320	0.062	25.03

Note. — Difference flux lightcurve for SM-2004-LMC-1060. See Table 2 for explanation of column headings.

Table 12. Lightcurve for SM-2004-LMC-1102

MJD	Rest Phase	Diff flux	flux err	$\frac{f_{VR}}{VR_{max}}$	$\frac{f_{VR}}{VR_{max}}$ err	S/N
53315.29	-40.2	-0.087	0.837	-0.003	9.605	0.10
53323.23	-33.7	-0.235	0.610	-0.007	2.591	0.39
53325.33	-31.9	-1.052	0.728	-0.033	0.693	1.45
53329.32	-28.7	0.401	0.741	0.013	1.849	0.54
53331.36	-27.0	-0.609	2.042	-0.019	3.355	0.30
53344.32	-16.4	0.643	0.836	0.020	1.301	0.77
53348.32	-13.1	6.190	0.602	0.196	0.104	10.28
53350.34	-11.4	9.280	3.479	0.293	0.377	2.67
53354.28	-8.2	27.495	3.617	0.869	0.137	7.60
53356.28	-6.6	25.415	1.013	0.803	0.054	25.08
53360.30	-3.3	29.460	0.950	0.931	0.049	31.01
53377.17	10.5	16.716	0.786	0.528	0.060	21.27
53381.15	13.8	12.371	0.758	0.391	0.072	16.33
53383.14	15.4	9.838	0.613	0.311	0.072	16.06
53387.17	18.7	8.589	0.611	0.271	0.080	14.05

Note. — Difference flux lightcurve for SM-2004-LMC-1102. See Table 2 for explanation of column headings.

Table 13. Spectroscopic Observations

SN ID	Telescope	Instrument	Date	Integration Time (s)
SM-2004-LMC-64	Magellan II	LDSS-2	2004-11-03	900
SM-2004-LMC-772	Magellan I	IMACS-4	2004-12-02	2400
SM-2004-LMC-797	Magellan I	IMACS-4	2004-12-02	2400
SM-2004-LMC-803	Magellan I	IMACS-4	2004-12-02	2700
SM-2004-LMC-811	Magellan I	IMACS-4	2004-12-02	2700
SM-2004-LMC-917	Magellan I	IMACS-4	2004-12-10	1800
SM-2004-LMC-944	Magellan II	LDSS-2	2004-12-18	2400
SM-2004-LMC-1002	Magellan II	LDSS-2	2004-12-17	2100
SM-2004-LMC-1052	Magellan II	LDSS-2	2004-12-18	2400
SM-2004-LMC-1060	Magellan II	LDSS-2	2005-01-11	1200
SM-2004-LMC-1102	Magellan II	LDSS-2	2005-01-09	3600

Table 14. Redshifts from Galaxy Features

SN ID	galaxy features	galaxy z	SN z
SM-2004-LMC-1002	CaI H&K, Hβ	0.35	0.35
SM-2004-LMC-1052	CaII H&K, OIII, Hβ, OII, Hγ	0.348	0.34
SM-2004-LMC-1060	CaII H&K, OIII, Hβ, OII, Hγ	0.154	0.16

Note. — Sources exhibiting strong galactic features. *SN ID* indicates the SN whose spectrum shows strong galaxy features. *Galaxy features* lists the observed features. *Galaxy z* gives the redshift determined from the galaxy lines. *SN z* gives the redshift determined through the nearby SN comparison method described in Section 3.2.

Table 15. Best Fit Parameters

Fit Description	$\chi^2/d.o.f.$	$d.o.f.$	t_r (days)	n (days)	m (days)	τ (days)	γ	s_{797}	s_{803}
Functional Fit (no stretch)[a]	1.16	38	-22.2±0.6	9.8±0.8	8.3±1.4	15.2±0.6	0.0029±0.0005	···	···
Functional Fit (with stretch)[b]	0.97	36	-19.2±1.3	13.8±1.3	8.4±1.5	14.0±0.8	0.0030±0.0006	0.92±0.02	1.01±0.02

[a]Functional Model of SN Ia described in Section 4.1 without stretch parameters to standardize lightcurve width.

[b]Functional Model of SN Ia with stretch parameters to normalize widths of SNe in composite lightcurve. Fit normalized to SM-2004-LMC-944.

Note. — Summary of best fit parameters from fits described in Section 4.1. The fits are performed on the observed VR-band $\frac{f_{VR}}{VR_{max}}$ composite lightcurve shifted in time to the SN rest-frame. The composite lightcurve includes four SNe Ia with z = 0.135–0.165. See Section 4.3 for description of composite lightcurve construction.

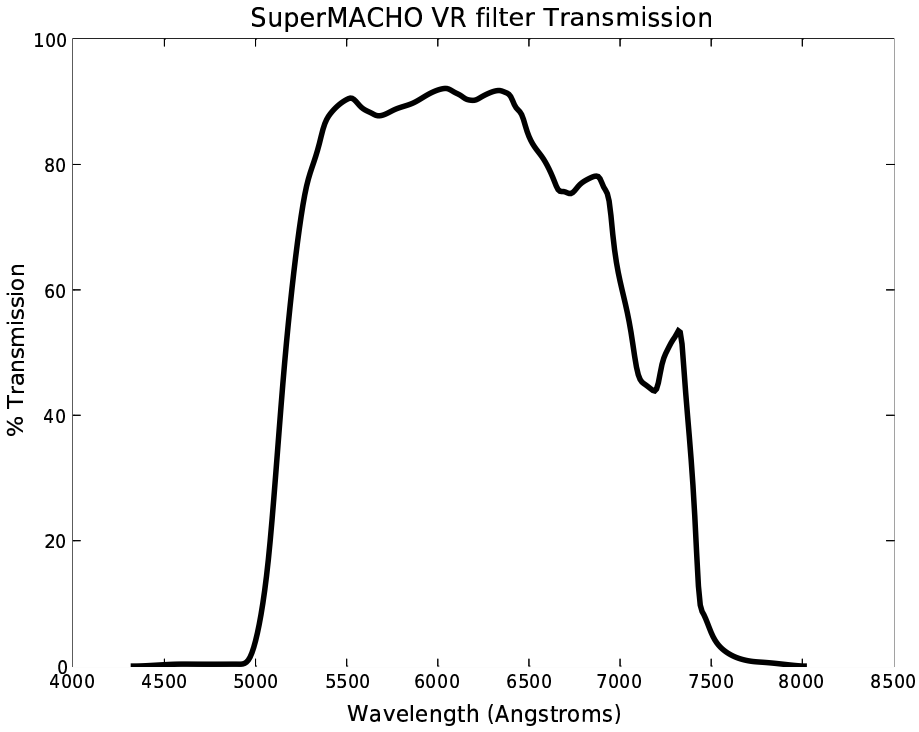

Fig. 1.— Transmission curve for the SuperMACHO VR filter. An electronic table of the transmission curve can be found at http://ctiokw.ctio.noao.edu/supermacho/SNrise.

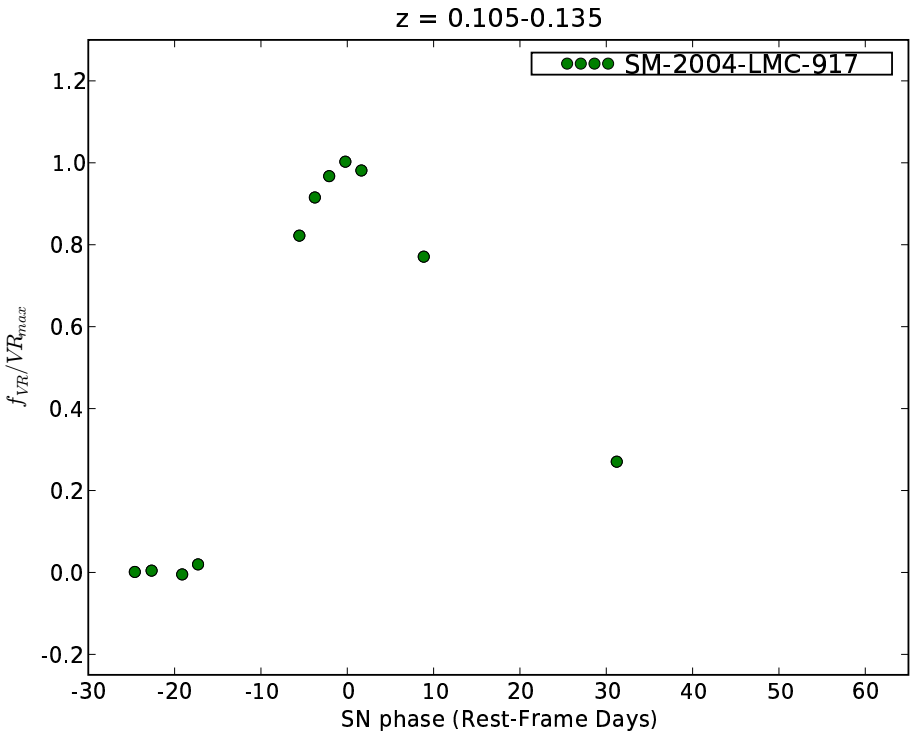

Fig. 2.— Restframe VR-band lightcurve of SM-2004-LMC-917 which has a redshift of 0.11. Data is shown in flux units normalized to the flux at maximum brightness. Error bars represent 1σ errors. Where error bars are not seen, 1σ errors are smaller than symbol.

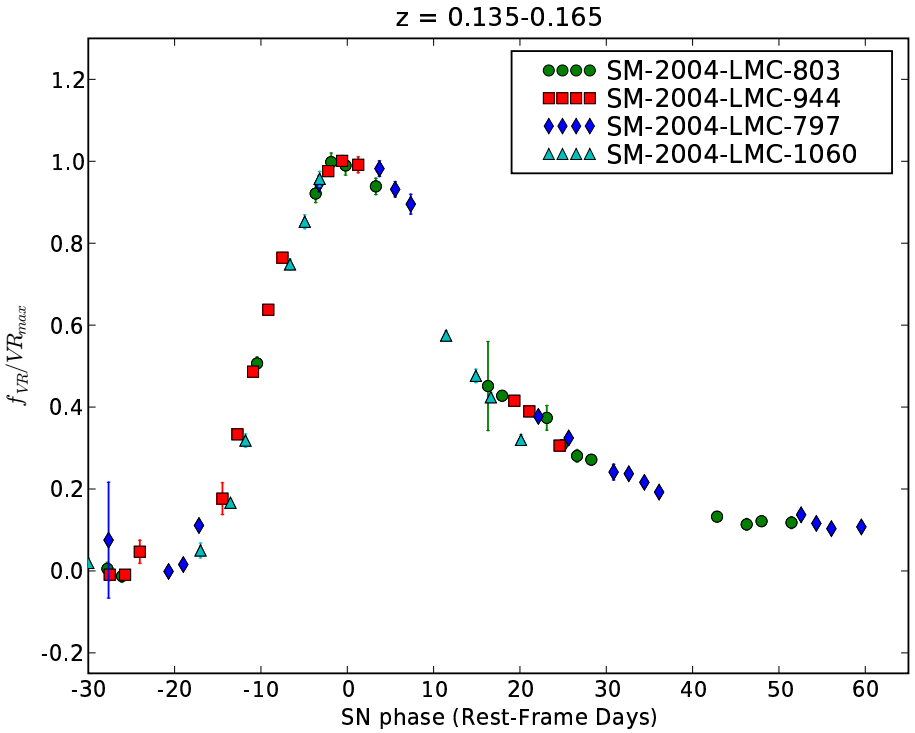

Fig. 3.— Restframe VR lightcurves of SNe Ia at z = 0.135–0.165. Data is shown in flux units normalized to the flux at maximum brightness. Error bars represent 1σ errors. Where error bars are not seen, 1σ errors are smaller than symbol. SM-2004-LMC-803 (circles) has a redshift of 0.16. SM-2004-LMC-944 (squares) has a redshift of 0.15. SM-2004-LMC-797 (diamonds) has a redshift of 0.145. SM-2004-LMC-1060 (triangles) has a redshift of 0.154.

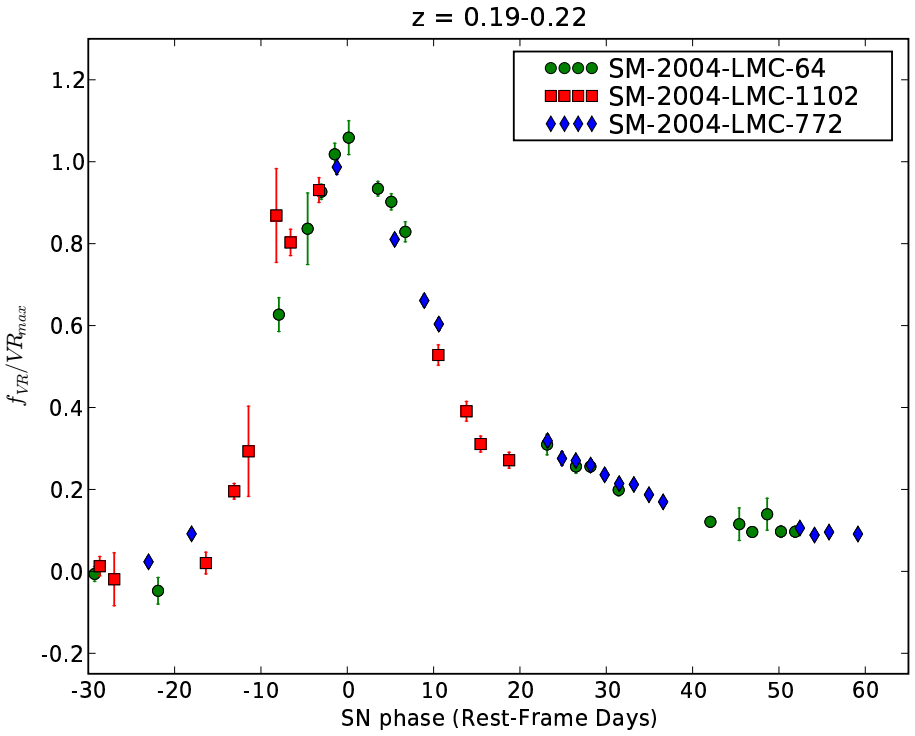

Fig. 4.— Restframe VR lightcurves of SNe Ia at z = 0.19–0.22. Error bars represent 1σ errors. Where error bars are not seen, 1σ errors are smaller than symbol. SM-2004-LMC-64 (circles) has a redshift of 0.22. SM-2004-LMC-1102 (squares) has a redshift of 0.22. SM-2004-LMC-772 (diamonds) has a redshift of 0.19.

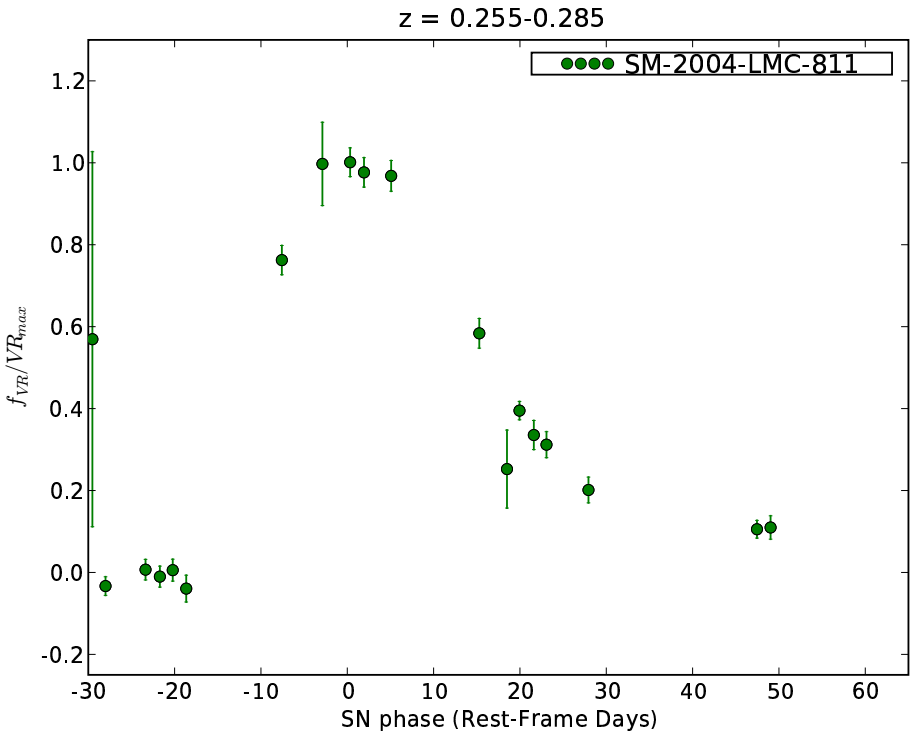

Fig. 5.— Restframe VR lightcurve of SM-2004-LMC-811 which has a redshift of 0.27. Data is shown in flux units normalized to the flux at maximum brightness. Error bars represent 1σ errors. Where error bars are not seen, 1σ errors are smaller than symbol.

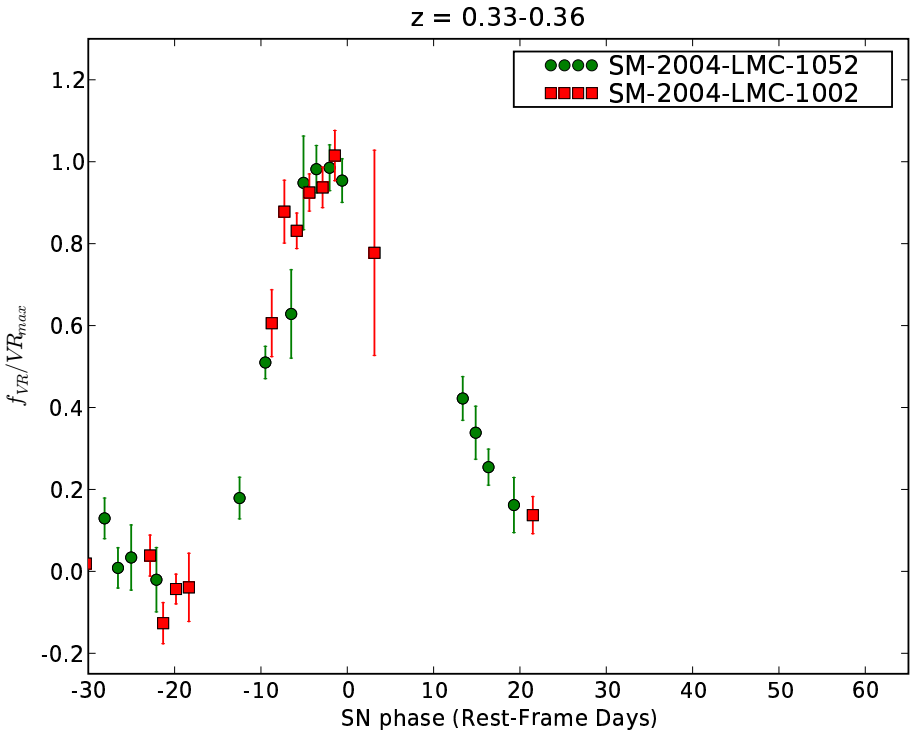

Fig. 6.— Restframe VR lightcurves of SNe Ia at z = 0.33–0.36. Data is shown in flux units normalized to the flux at maximum brightness. Error bars represent 1σ errors. Where error bars are not seen, 1σ errors are smaller than symbol. SM-2004-LMC-1052 (circles) has a redshift of 0.348. SM-2004-LMC-1002 (squares) has a redshift of 0.35.

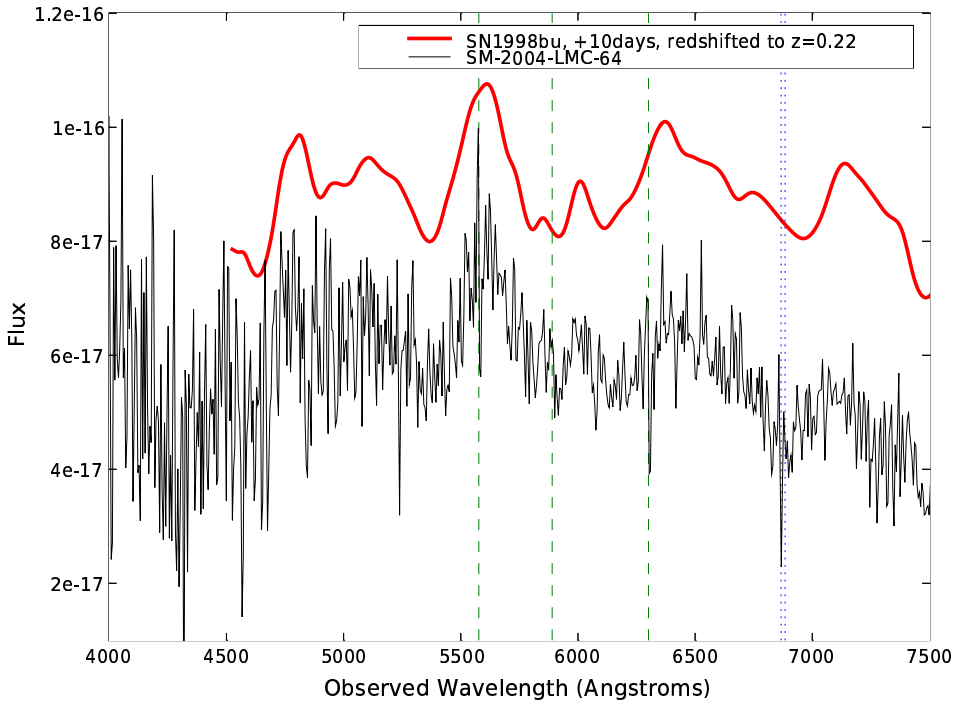

Fig. 7.— Flux-calibrated spectrum of SM-2004-LMC-64 with comparison nearby spectrum of SN1998bu above. The spectrum of SN1998bu was taken at +10 days relative to B-band maximum and is shown redshifted to z = 0.22. The flux of the comparison spectrum has been smoothed, scaled, and offset. Dashed lines indicate sky emission lines at 5577Å, 5890Å, and 6301Å. Dotted lines demark the atmospheric O_2-band between 6867–6884Å. Electronic data tables can be found at http://ctiokw.ctio.noao.edu/supermacho/SNrise.

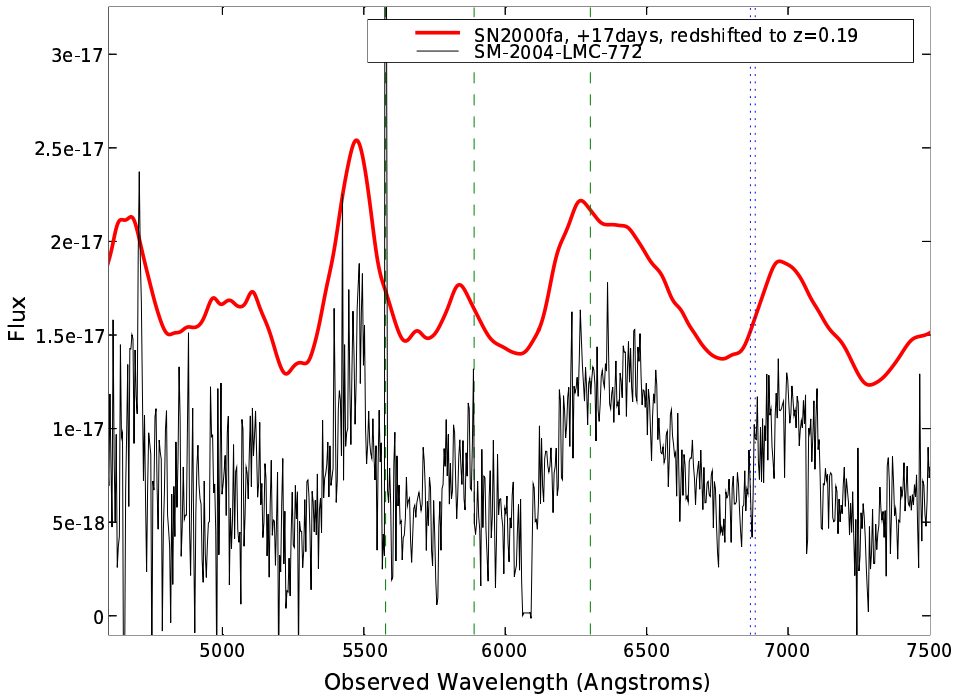

Fig. 8.— Flux-calibrated spectrum of SM-2004-LMC-772 with comparison nearby spectrum of SN2000fa above. The spectrum of SN2000fa was taken at +17 days relative to B-band maximum and is shown redshifted to z = 0.19. The flux of the comparison spectrum has been smoothed, scaled, and offset. See Figure 7 for explanation of dashed and dotted lines.

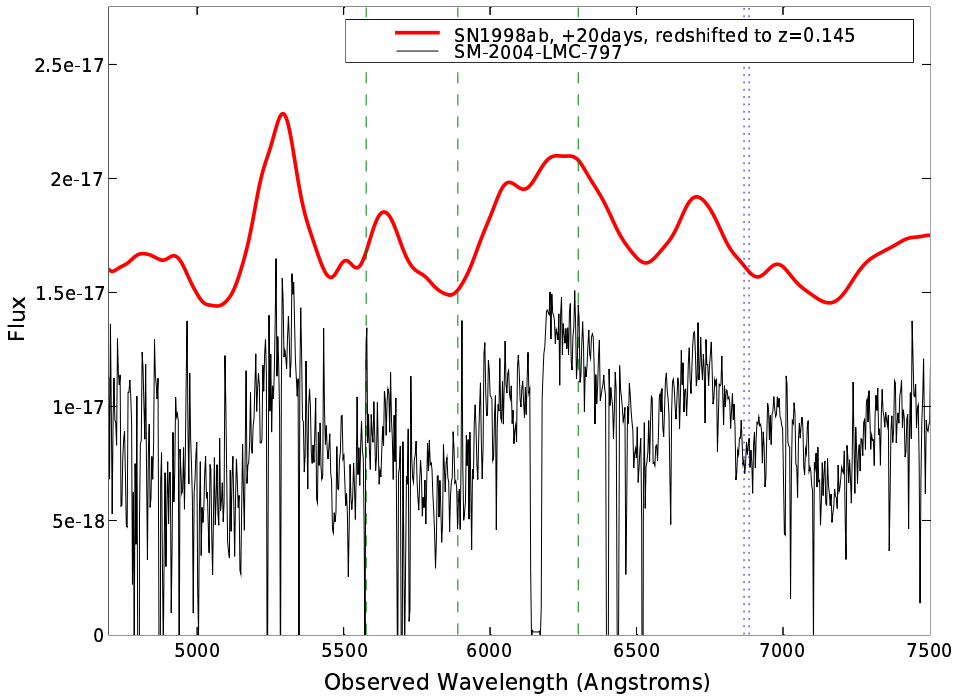

Fig. 9.— Flux-calibrated spectrum of SM-2004-LMC-797 with comparison nearby spectrum of SN1998ab above. The spectrum of SN1998ab was taken at +20 days relative to B-band maximum and is shown redshifted to z = 0.145. The flux of the comparison spectrum has been smoothed, scaled, and offset. See Figure 7 for explanation of dashed and dotted lines.

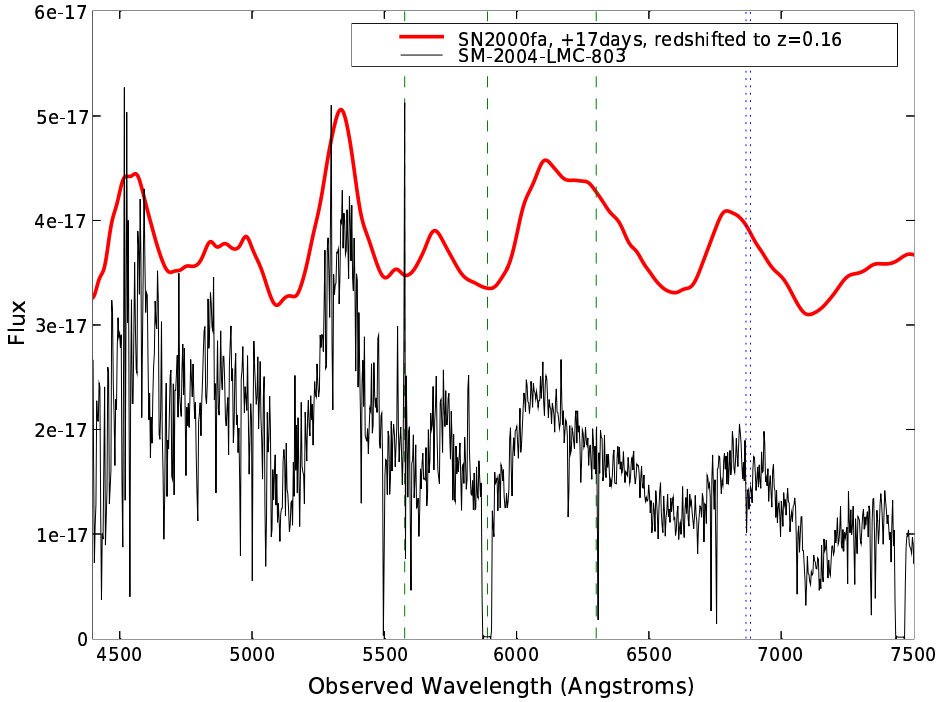

Fig. 10.— Flux-calibrated spectrum of SM-2004-LMC-803 with comparison nearby spectrum of SN2000fa above. The spectrum of SN2000fa was taken at +17 days relative to B-band maximum and is shown redshifted to z = 0.16. The flux of the comparison spectrum has been smoothed, scaled, and offset. See Figure 7 for explanation of dashed and dotted lines.

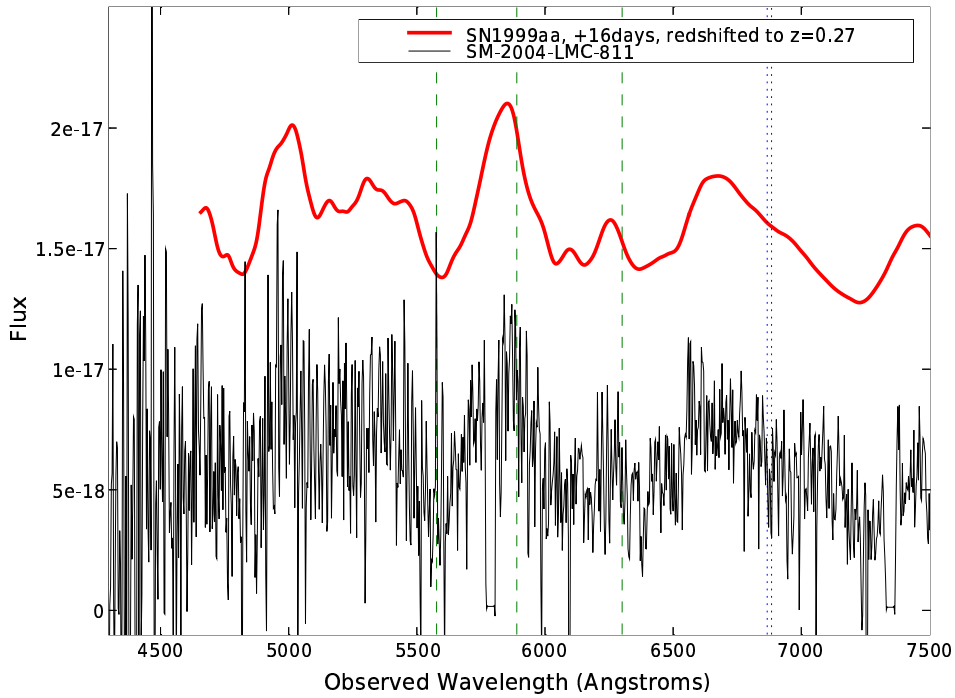

Fig. 11.— Flux-calibrated spectrum of SM-2004-LMC-811 with comparison nearby spectrum of SN1999aa above. The spectrum of SN1999aa was taken at +16 days relative to B-band maximum and is shown redshifted to z = 0.27. The flux of the comparison spectrum has been smoothed, scaled, and offset. See Figure 7 for explanation of dashed and dotted lines.

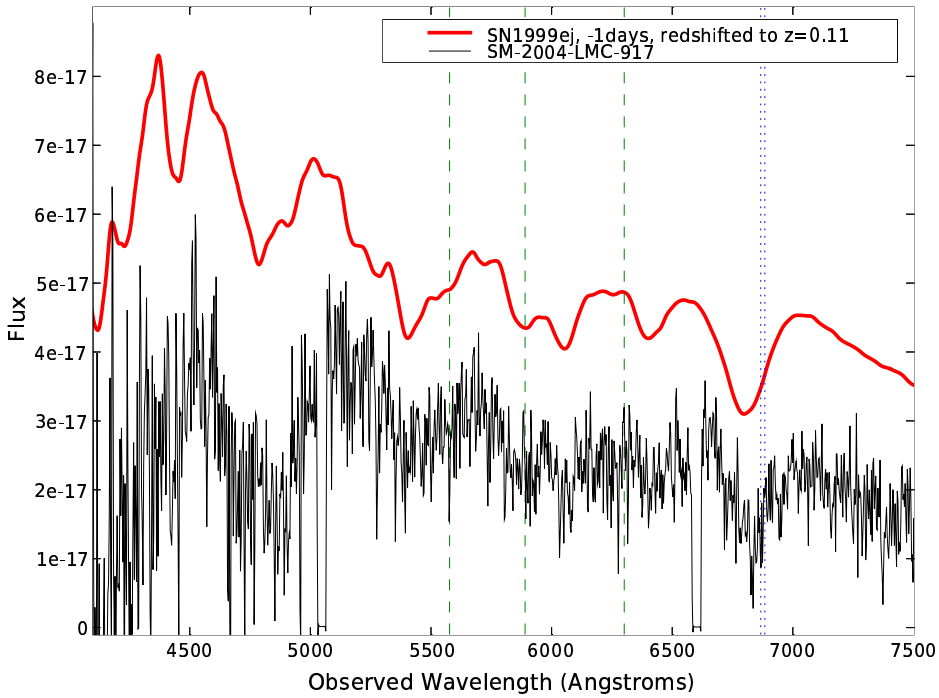

Fig. 12.— Flux-calibrated spectrum of SM-2004-LMC-917 with comparison nearby spectrum of SN1999ej above. The spectrum of SN1999ej was taken at -1 days relative to B-band maximum and is shown redshifted to z = 0.11. The flux of the comparison spectrum has been smoothed, scaled, and offset. See Figure 7 for explanation of dashed and dotted lines.

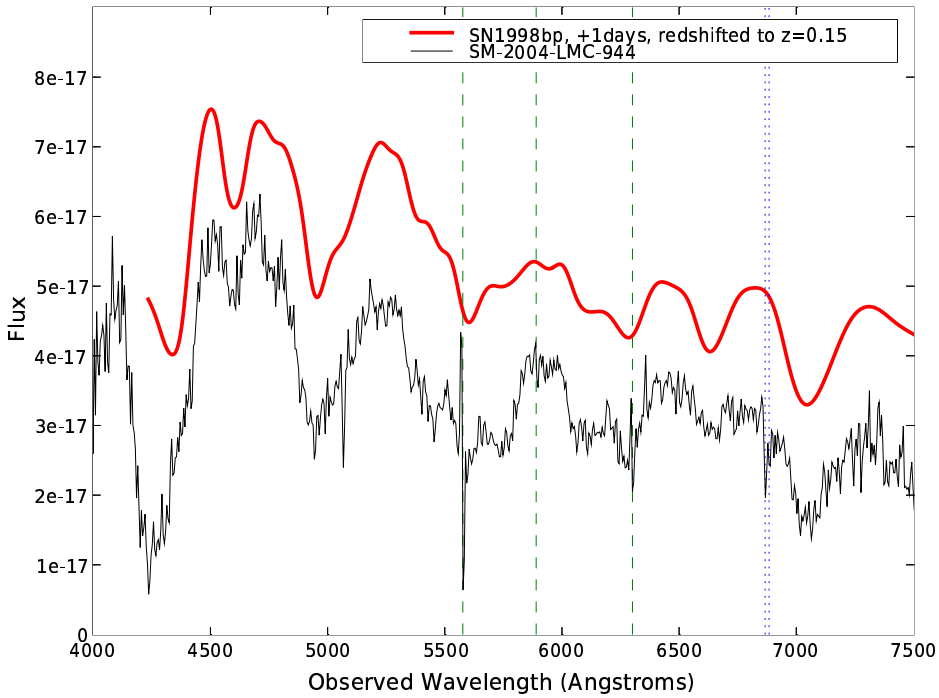

Fig. 13.— Flux-calibrated spectrum of SM-2004-LMC-944 with comparison nearby spectrum of SN1998bp above. The spectrum of SN1998bp was taken at +1 days relative to B-band maximum and is shown redshifted to z = 0.15. The flux of the comparison spectrum has been smoothed, scaled, and offset. See Figure 7 for explanation of dashed and dotted lines.

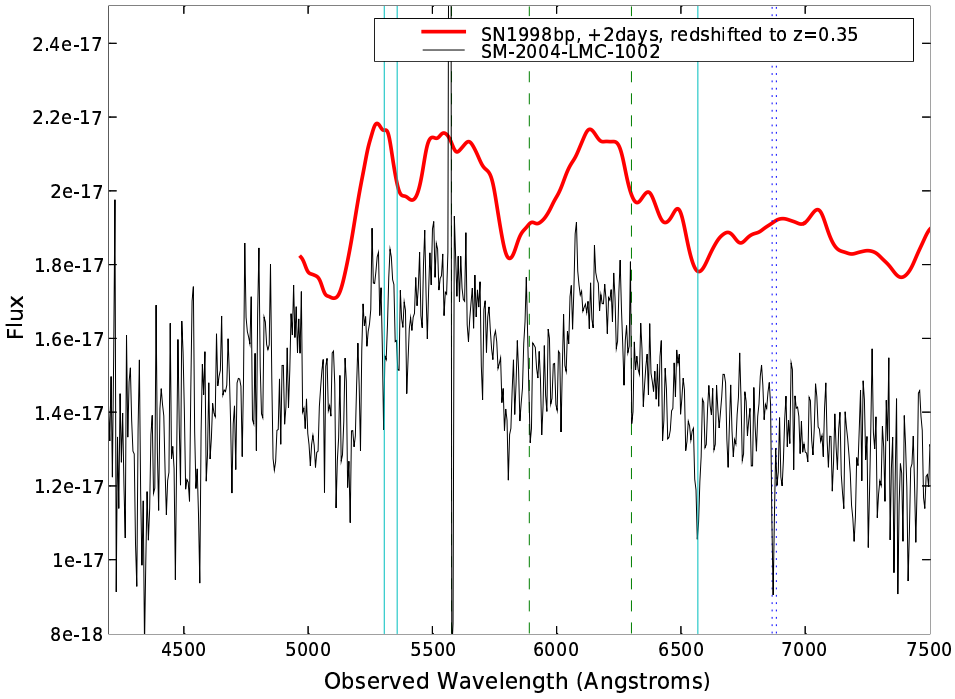

Fig. 14.— Flux-calibrated spectrum of SM-2004-LMC-1002 with comparison nearby spectrum of SN1998bp above. The spectrum of SN1998bp was taken at +2 days relative to B-band maximum and is shown redshifted to z = 0.35. The flux of the comparison spectrum has been smoothed, scaled, and offset. Solid lines mark galaxy features used to independently find the source redshift of z = 0.350. See Figure 7 for explanation of dashed and dotted lines.

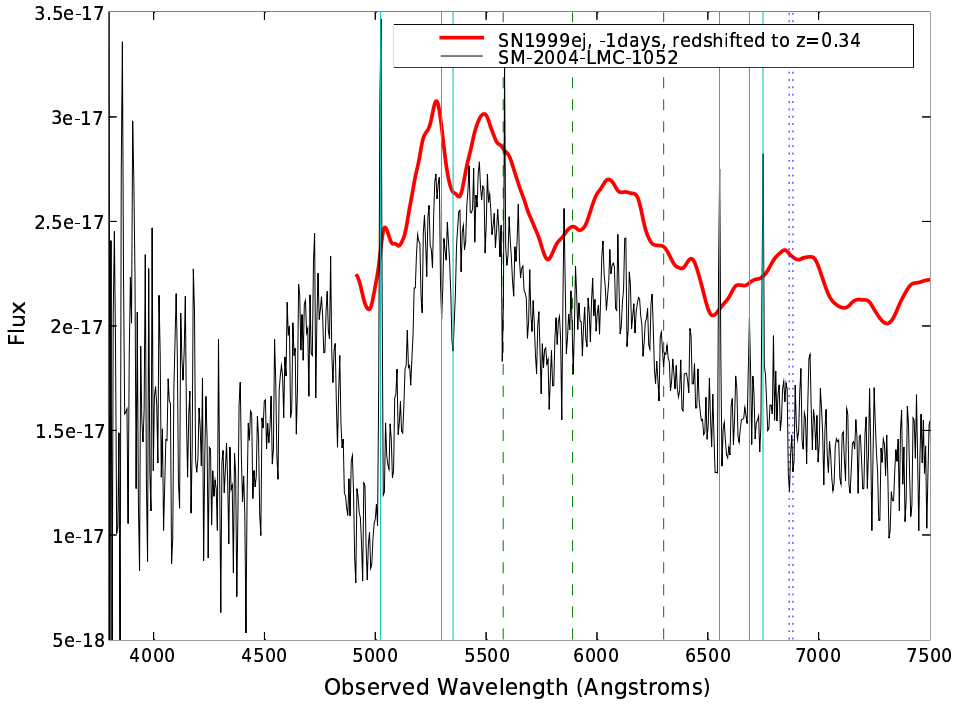

Fig. 15.— Flux-calibrated spectrum of SM-2004-LMC-1052 with comparison nearby spectrum of SN1999ej above. The spectrum of SN1999ej was taken at -1 days relative to B-band maximum and is shown redshifted to z = 0.34. The flux of the comparison spectrum has been smoothed, scaled, and offset. Solid lines mark galaxy features used to independently find the source redshift of z = 0.348. See Figure 7 for explanation of dashed and dotted lines.

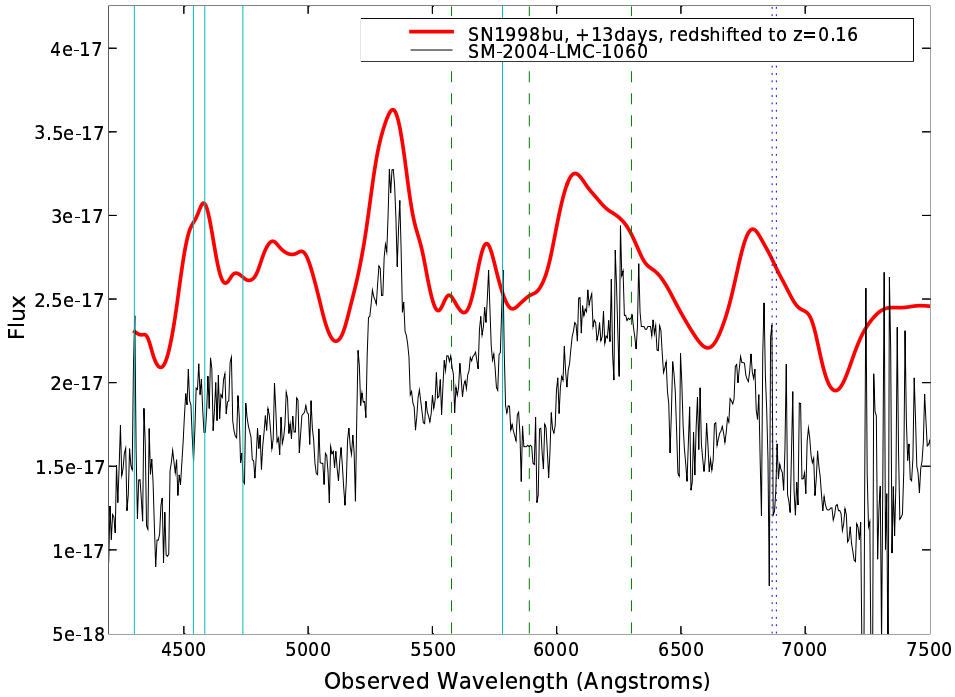

Fig. 16.— Flux-calibrated spectrum of SM-2004-LMC-1060 with comparison nearby spectrum of SN1998bu above. The spectrum of SN1998bu was taken at +13 days relative to B-band maximum and is shown redshifted to z = 0.16. The flux of the comparison spectrum has been smoothed, scaled, and offset. Solid lines mark galaxy features used to independently find the source redshift of z = 0.154. See Figure 7 for explanation of dashed and dotted lines.

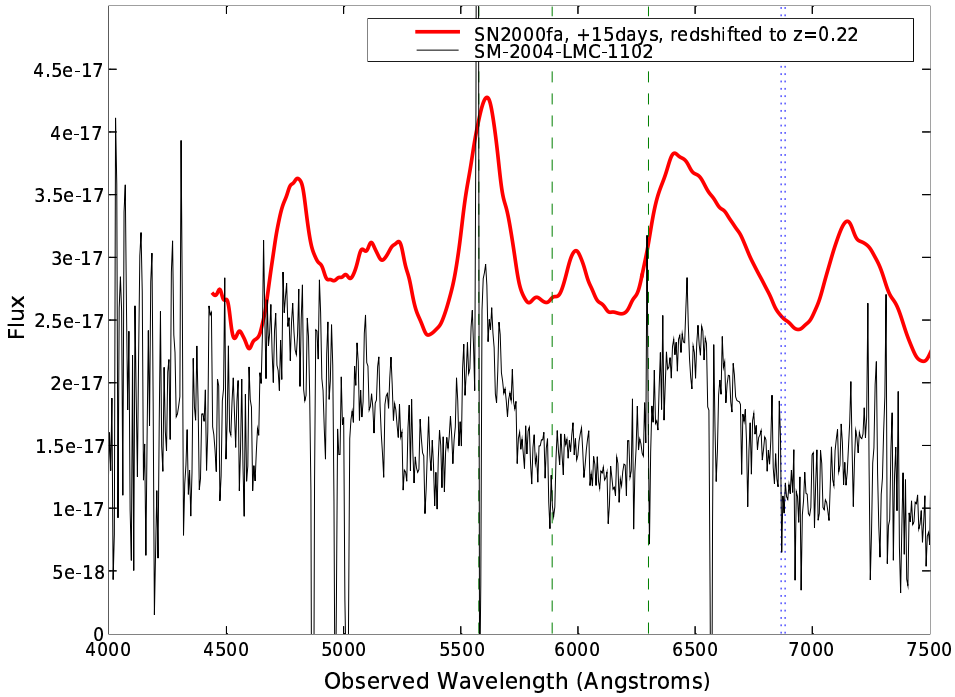

Fig. 17.— Flux-calibrated spectrum of SM-2004-LMC-1102 with comparison nearby spectrum of SN2000fa above. The spectrum of SN2000fa was taken at +15 days relative to B-band maximum and is shown redshifted to z = 0.22. The flux of the comparison spectrum has been smoothed, scaled, and offset. See Figure 7 for explanation of dashed and dotted lines.

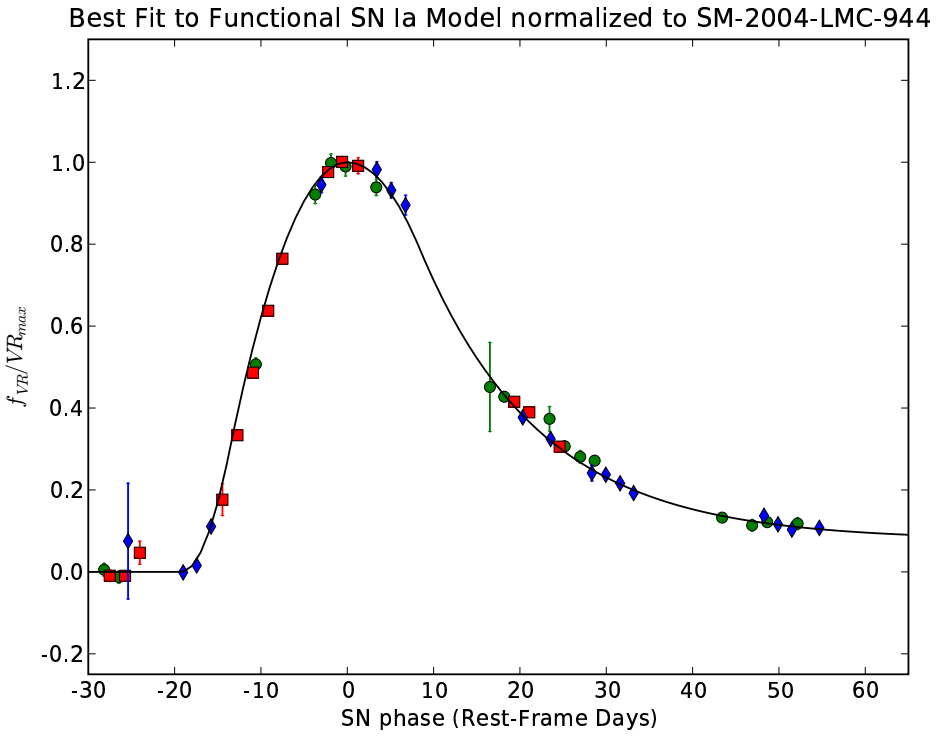

Fig. 18.— The best fit of the functional SN Ia model described in Section 4.1 to the composite lightcurve. Stretch parameters were added to normalize the width of the lightcurve to that of SM-2004-LMC-944 (squares). The lightcurve shown has a Δm_{-10} in the VR-band of 0.52. For SM-2004-LMC-803 (circles), the stretch parameter is 1.01. For SM-2004-LMC-797, the stretch parameter is 0.92. Table 15 gives the parameters and their uncertainties for this fit.